



**COMPUTER MODELING OF A ROTATING  
DETONATION ENGINE IN A ROCKET  
CONFIGURATION**

THESIS

Nihar N. Shah, 1st Lt, USAF  
AFIT-ENY-MS-15-M-230

**DEPARTMENT OF THE AIR FORCE  
AIR UNIVERSITY**

**AIR FORCE INSTITUTE OF TECHNOLOGY**

**Wright-Patterson Air Force Base, Ohio**

DISTRIBUTION STATEMENT A  
APPROVED FOR PUBLIC RELEASE; DISTRIBUTION UNLIMITED.

The views expressed in this document are those of the author and do not reflect the official policy or position of the United States Air Force, the United States Department of Defense or the United States Government. This material is declared a work of the U.S. Government and is not subject to copyright protection in the United States.

AFIT-ENY-MS-15-M-230

COMPUTER MODELING OF A ROTATING DETONATION ENGINE IN A ROCKET  
CONFIGURATION

THESIS

Presented to the Faculty  
Department of Aeronautics and Astronautics  
Graduate School of Engineering and Management  
Air Force Institute of Technology  
Air University  
Air Education and Training Command  
in Partial Fulfillment of the Requirements for the  
Degree of Master of Science in Aeronautical Engineering

Nihar N. Shah, B.S.

1st Lt, USAF

March 2015

DISTRIBUTION STATEMENT A  
APPROVED FOR PUBLIC RELEASE; DISTRIBUTION UNLIMITED.

COMPUTER MODELING OF A ROTATING DETONATION ENGINE IN A ROCKET  
CONFIGURATION

THESIS

Nihar N. Shah, B.S.  
1st Lt, USAF

Committee Membership:

Dr. P. I. King  
Chair

Dr. F. R. Schauer  
Member

Maj D. Liu, PhD  
Member

## Abstract

Detonation-based combustors leverage the higher thermodynamic efficiency of the Atkinson cycle compared to the traditional deflagration-based combustion of the Brayton cycle. The rotating detonation engine (RDE) has one or more shock waves rotating around an annulus. The RDE can theoretically be 20% more thermally efficient than a traditional deflagration-based cycle. An RDE was modeled in Numerical Propulsion System Simulation (NPSS) based on a model developed in Microsoft Excel. The thermodynamic analysis of the RDE in these models is broken into four streams. Empirical models were used to find the percentage of the total flow in each stream. The pre-detonation pressure was iterated until the entrance mass flow calculations matched the exit mass flow calculations. A parametric analysis was used to compare the variation in specific impulse from the NPSS model to the Microsoft Excel model and other published results. The RDE has a peak air-breathing engine specific impulse of approximately 5,500 *sec* and a peak rocket engine specific impulse of approximately 150 *sec*.

## Acknowledgements

*Somewhere, something incredible is waiting to be known. – Carl Sagan*

I want to thank Mr. Tom Kaemming for paving the way for the work in this thesis and being patient with me as I learned his model. I would also like to thank Maj Ionio Andrus for the mentoring he provided throughout my studies. I want to thank my advisor, Dr. King, for the time and effort he invested into my work and the guidance he provided throughout the process. Finally, I would like to thank my friends and family for their support throughout my career.

Nihar N. Shah

# Contents

	Page
Abstract . . . . .	iv
Acknowledgements . . . . .	v
Nomenclature . . . . .	viii
Variables . . . . .	viii
Subscripts . . . . .	xi
Acronyms . . . . .	xii
List of Figures . . . . .	xiii
I. Introduction . . . . .	1
Problem . . . . .	3
Methodology . . . . .	3
II. Previous Work on Rotating Detonation Engines . . . . .	4
Station Designation . . . . .	4
Thermodynamic Overview . . . . .	5
Empirical Models . . . . .	8
Plenum Model . . . . .	8
Detonation Height Ratio Empirical Models . . . . .	9
Summary . . . . .	13
III. Model Summary . . . . .	14
RDE Element Summary . . . . .	14
Initial Calculations . . . . .	18
Geometric Parameters . . . . .	18
Gas Properties . . . . .	18
Entrance Flow Model . . . . .	21
Thermodynamics Model . . . . .	28
Path <i>a</i> : Detonation Only . . . . .	28
Path <i>b</i> : Detonation and Shock . . . . .	32
Path <i>c</i> : Deflagration . . . . .	33
Path <i>d</i> : Mixed Flow . . . . .	36
Exit Flow Model . . . . .	37
Mass Flow . . . . .	38
Summary . . . . .	38

	Page
IV. Analysis and Results .....	39
Verification .....	39
Comparison to Published Results .....	42
Model Application .....	44
Investigative Questions Answered .....	53
Summary .....	54
V. Conclusions and Recommendations .....	55
Recommendations for Future Research .....	55
Model Development .....	55
Model Application .....	56
Summary .....	56
Appendix A. Summary of Implemented Functions .....	58
References .....	64
Vita .....	66

## Nomenclature

<b>Variable</b>	<b>Definition</b>
$3^*$	Entrance to RDE
4	RDE exit
8	Nozzle
9	Nozzle exit
$A$	Area
$a$	Speed of sound ( $\frac{ft}{sec}$ )
$A^*$	Throat area for choked flow ( $ft^2$ )
$A_3$	Cross-sectional throughflow area per detonation wave ( $ft^2$ )
$\left(\frac{A_{3.4}}{A_{3.2}}\right)_{CJ}$	Detonation lateral area relief
$\frac{A_8}{A_3}$	Combustion chamber area contraction
$\frac{A_9}{A_8}$	Nozzle area ratio
$\frac{A_{inj}}{A_3}$	Injector-to-throat area ratio
$a_t$	Speed of sound using total temperature ( $\frac{ft}{sec}$ )
$b$	Percent pressure drop
$C_{eff}$	Effective circumference per detonation wave ( $mm^2$ )
$C_{W3}$	Station 3 flow coefficient
$C_{W8}$	RDE exit flow coefficient
$C_P$	Specific heat capacity at constant pressure ( $\frac{J}{kg-K}$ )
$C_S$	Nozzle stream thrust coefficient
$D$	Detonation wave speed in laboratory frame-of-reference ( $\frac{ft}{sec}$ )
$D_i$	RDE inner diameter ( $mm$ )
$D_m$	RDE mean throughflow diameter ( $mm$ )
$D_o$	RDE outer diameter ( $mm$ )
$\frac{F}{\dot{m}}$	Specific thrust ( $\frac{lb_f}{lb_m/sec}$ )
$FAR$	Fuel-to-air ratio
$g_0$	Standard gravity ( $\frac{ft}{sec^2}$ )
$g_c$	Conversion factor ( $\frac{lb_m-ft}{lb_f-sec^2}$ )
$H$	Heat addition due to combustion ( $kJ$ )
$\Delta H$	Heat of combustion ( $\frac{kJ}{kg-K}$ )
$\Delta H_v$	Heat of combustion, referenced to fuel flow ( $\frac{kJ}{kg-K}$ )
$\Delta H_{stoich}$	Heat of combustion, referenced to stoichiometric mix ( $\frac{kJ}{kg-K}$ )
$\Delta h_{fill}$	Incremental fill height ( $in$ )
$h_{det}$	Detonation height ( $in$ )
$h_{RDE}$	RDE height ( $in$ )

Variable	Definition
$I_{sp}$	Specific thrust ( $sec$ )
$k$	Time constant in empirical model ( $\frac{1}{sec}$ )
$M$	Mach number
$\dot{m}$	Mass flow rate ( $\frac{lb_m}{sec}$ )
$\Delta m$	Incremental mass ( $lb_m$ )
$\frac{m}{m^*}$	Mass correction factor
$\frac{mV}{mV^*}$	Momentum correction factor
$MFP$	Mass flow parameter with total pressure ( $\frac{sec\sqrt{R}}{ft}$ )
$MFp$	Mass flow parameter with static pressure ( $\frac{sec\sqrt{R}}{ft}$ )
$MW$	Molecular weight ( $\frac{kg}{kmol}$ )
$n_{waves}$	Number of detonation waves in RDE chamber
$P$	Static pressure ( $psia$ )
$P_0$	Ambient pressure ( $psia$ )
$\left(\frac{P_{3.4}}{P_{3.2}}\right)_{det}$	Ratio of static pressures across detonation
$P_t$	Total pressure
path $a$	Flowpath going through detonation only
path $b$	Flowpath going through detonation and oblique shock
path $c$	Flowpath going through deflagration and oblique shock
path $d$	Flowpath containing mixed flow
$q$	Non-dimensional heat addition term
$R$	Specific gas constant ( $\frac{J}{kg-K}$ )
$R_U$	Universal gas constant ( $\frac{J}{kmol-K}$ )
$S$	Entropy ( $\frac{J}{K}$ )
$S_t$	Total entropy ( $\frac{J}{R}$ )
$T$	Static temperature ( $R$ )
$\Delta t$	Discretized time step ( $sec$ )
$t_{cycle}$	Duration of detonation cycle ( $sec$ )
$T_t$	Total temperature ( $R$ )
$U_{wave}$	Azimuthal wave velocity ( $\frac{ft}{sec}$ )
$V$	Time-averaged flow velocity ( $\frac{ft}{sec}$ )
$V_{avg}$	Mass-averaged velocity distortion ( $\frac{ft}{sec}$ )
$V_{defl,std}$	Deflagration flame speed at standard conditions ( $\frac{ft}{sec}$ )
$V_{max}$	Maximum velocity distortion ( $\frac{ft}{sec}$ )
$V_{min}$	Minimum velocity distortion ( $\frac{ft}{sec}$ )
$W_1$	Flow upstream of detonation wave in detonation wave frame-of-reference ( $\frac{ft}{sec}$ )
$W_2$	Flow downstream of detonation wave in detonation wave frame-of-reference ( $\frac{ft}{sec}$ )
$X$	Mole fraction
$Z$	Percentage of flow, by mass
$\gamma$	Ratio of specific heats

<b>Variable</b>	<b>Definition</b>
$\theta_{shock}$	Oblique shock angle relative to flow ( $^{\circ}$ )
$\nu$	Specific volume $\left(\frac{1}{ft^3}\right)$
$\pi_b$	Pressure ratio across RDE
$\tau$	RDE channel width ( $mm$ )
$\tau_{drop}$	Time until first drop ( $sec$ )

<b>Subscript</b>	<b>Definition</b>
3.2	Pre-combustion region
3.4	Post-detonation flow
4	Exit of RDE
8	Nozzle
9	Nozzle exit
<i>a</i>	Flow traveling along path <i>a</i>
<i>a</i> 3.4	Post-detonation flow traveling along path <i>a</i>
<i>a</i> 4	Flowpath <i>a</i> at RDE exit
<i>amb</i>	Ambient
<i>avg</i>	Average
<i>b</i>	Flow traveling along path <i>b</i>
<i>b</i> 3.4	Post-detonation flow traveling along path <i>b</i>
<i>b</i> 3.6	Post-shock flow traveling along path <i>b</i>
<i>b</i> 4	Flowpath <i>b</i> at RDE exit
<i>bwd</i>	Backward
<i>c</i>	Flow traveling along path <i>c</i>
$C_2H_4$	Ethylene
<i>c</i> 3.4	Post-deflagration flow traveling along path <i>c</i>
<i>c</i> 3.6	Post-shock flow traveling along path <i>c</i>
<i>d</i>	Flow traveling along path <i>d</i>
<i>d</i> 3.6	Mixed region containing flow from paths <i>a</i> , <i>b</i> , and <i>c</i>
<i>d</i> 4	Flowpath <i>d</i> at RDE exit
<i>defl</i>	Deflagration
<i>det</i>	Detonation
<i>fwd</i>	Forward
$H_2$	Hydrogen
<i>inj</i>	Injector
$P$	Products
$R$	Reactants
<i>std</i>	At standard conditions
<i>stoich</i>	Stoichiometric
<i>sum</i>	Summation
<i>tot</i>	Total
$w$	Detonation wave frame-of-reference
$x$	Azimuthal direction
$y$	Axial direction

<b>Acronym</b>	<b>Definition</b>
CEA	Chemical Equilibrium with Applications
CFD	Computational fluid dynamics
JANNAF	Joint Army Navy NASA Air Force
NASA	National Aeronautics and Space Administration
NPSS	Numerical Propulsion System Simulation
RDE	Rotating detonation engine
SAE	Society of Automotive Engineers
ZND	Zel'dovich, von Neumann, and Döring

## List of Figures

Figure		Page
1	Comparison of thermodynamic diagrams for Brayton and Atkinson cycles [1] .....	2
2	Temperature contour plot of an RDE simulation [2: Figure 1] .....	2
3	Two-dimensional “unwrapped” temperature contour plot of the RDE [3: Fig. 2] .....	3
4	Station designations used in rocket configuration[4: Fig. 3-1] .....	4
5	Velocity triangles used to change between laboratory frame-of-reference and detonation wave frame-of-reference [5: Fig. 5] .....	5
6	Two-dimensional “unrolled” RDE with tracked pathlines and three thermal regions [3: Fig. 8] .....	6
7	Path and substation nomenclature [4: Fig. 7-2] .....	7
8	Comparison of pressure profile from computational fluid dynamics (CFD) results to model from Eq. 1 and Eq. 2 [4: Fig. 6-1; 3: Fig. 9] .....	10
9	Empirical models based on the ratio of detonation height to RDE height .....	11
10	Correction factor for the mass ( $m/m^*$ ) and momentum ( $mV/mV^*$ ) .....	13
11	Summary of RDE element implementation [4: Fig. 5-1] .....	15
12	Parametric variation of RDE height and specific impulse ( $D_m = 140\text{ mm}$ , $P_{t3} = 58.784\text{ psia}$ , and $T_{t3} = 540\text{ R}$ ) .....	40
13	Parametric variation of mean throughflow diameter and specific impulse ( $h_{RDE} = 237\text{ mm}$ , $P_{t3} = 58.784\text{ psia}$ , and $T_{t3} = 540\text{ R}$ ) .....	40
14	Parametric variation of entrance pressure and specific impulse ( $h_{RDE} = 237\text{ mm}$ , $D_m = 140\text{ mm}$ , and $T_{t3} = 540\text{ R}$ ) .....	41

Figure	Page
15 Parametric variation of entrance temperature and specific impulse ( $h_{RDE} = 237 \text{ mm}$ , $D_m = 140 \text{ mm}$ , and $P_{t3} = 58.784 \text{ psia}$ ) .....	41
16 Comparison of the RDE height variation from NPSS model to published results ( $D_m = 140 \text{ mm}$ , $P_{t3} = 58.784 \text{ psia}$ , and $T_{t3} = 540 \text{ R}$ ) .....	42
17 Comparison of the RDE mean throughflow diameter variation from NPSS model to published results ( $h_{RDE} = 237 \text{ mm}$ , $P_{t3} = 147 \text{ psia}$ , and $T_{t3} = 540 \text{ R}$ ) .....	43
18 Comparison of $P_{t3}/P_0$ from NPSS model to published results ( $h_{RDE} = 237 \text{ mm}$ , $D_m = 140 \text{ mm}$ , $P_0 = 14.7 \text{ psia}$ , and $T_{t3} = 540 \text{ R}$ ) .....	43
19 Parametric variation of entrance total pressure and entrance total temperature with the pre-combustion pressure ( $h_{RDE} = 237 \text{ mm}$ and $D_m = 140 \text{ mm}$ ) .....	44
20 Parametric analysis of shock angle with the exit total pressure and total temperature ( $h_{RDE} = 237 \text{ mm}$ , $D_m = 140 \text{ mm}$ , $P_{t3} = 58.784 \text{ psia}$ , and $T_{t3} = 540 \text{ R}$ ) .....	45
21 Parametric analysis of shock angle with the specific thrust and specific impulse ( $h_{RDE} = 237 \text{ mm}$ , $D_m = 140 \text{ mm}$ , $P_{t3} = 58.784 \text{ psia}$ , and $T_{t3} = 540 \text{ R}$ ) .....	46
22 Parametric analysis of RDE height and mean throughflow diameter on specific thrust ( $P_{t3} = 58.784 \text{ psia}$ , and $T_{t3} = 540 \text{ R}$ ) .....	47
23 Parametric analysis of RDE height and mean throughflow diameter on specific impulse ( $P_{t3} = 58.784 \text{ psia}$ , and $T_{t3} = 540 \text{ R}$ ) .....	47
24 Parametric analysis of RDE height and mean throughflow diameter on mass flow rate ( $P_{t3} = 58.784 \text{ psia}$ , and $T_{t3} = 540 \text{ R}$ ) .....	48
25 Parametric analysis of RDE height and mean throughflow diameter on thrust ( $P_{t3} = 58.784 \text{ psia}$ , and $T_{t3} = 540 \text{ R}$ ) .....	48
26 Parametric analysis of total entrance temperature and total pressure on specific thrust ( $h_{RDE} = 237 \text{ mm}$ and $D_m = 140 \text{ mm}$ ) .....	49

Figure		Page
27	Parametric analysis of total entrance temperature and total pressure on specific impulse ( $h_{RDE} = 237 \text{ mm}$ and $D_m = 140 \text{ mm}$ ) . . . . .	50
28	Parametric analysis of total entrance temperature and total pressure on mass flow rate ( $h_{RDE} = 237 \text{ mm}$ and $D_m = 140 \text{ mm}$ ) . . . . .	50
29	Parametric analysis of total entrance temperature and total pressure on thrust ( $h_{RDE} = 237 \text{ mm}$ and $D_m = 140 \text{ mm}$ ) . . . . .	51
30	Parametric analysis of total entrance temperature and total pressure on total exit temperature ( $h_{RDE} = 237 \text{ mm}$ and $D_m = 140 \text{ mm}$ ) . . . . .	51
31	Parametric variation of $\pi_b$ with total entrance pressure and total entrance temperature ( $h_{RDE} = 237 \text{ mm}$ and $D_m = 140 \text{ mm}$ ) . . . . .	52
32	Parametric variation of plenum pressure loss with total entrance pressure and total entrance temperature ( $h_{RDE} = 237 \text{ mm}$ and $D_m = 140 \text{ mm}$ ) . . . . .	53

# COMPUTER MODELING OF A ROTATING DETONATION ENGINE IN A ROCKET CONFIGURATION

## I. Introduction

Conventional jet and rocket engines extract energy from fuel using deflagration processes, which follow a Brayton cycle [6]. The efficiency of an ideal Brayton cycle depends on the ratio of temperatures at the entrance and exit of the process [6], so increasing the exit temperature increases the efficiency of the process. Material properties limit the maximum exhaust temperature, thus limiting efficiency [7].

A detonation cycle, however, follows an Atkinson cycle [8]. Figure 1 illustrates the thermodynamic nature of the Brayton and Atkinson cycles via the temperature-entropy ( $T$ - $S$ ) and pressure-specific volume ( $P$ - $\nu$ ) diagrams. The superior performance of the Atkinson is evidenced by the greater area under the two curves in Fig. 1. For equal heat addition and mechanical compression, the Atkinson cycle is more thermodynamically efficient than the Brayton cycle [8].

One utilization of a detonation cycle is the rotating detonation engine (RDE). Research into the RDE began as early as the 1950s at the Lavrentyev Institute of Hydrodynamics in Siberia [9]. A major motivator for the study of RDEs is their increased thermal efficiency; the RDE can theoretically be 20% more efficient than a traditional deflagration-based cycle [2; 10; 11].

In an RDE, one or more shock waves rotate around an annulus. Figure 2 illustrates a temperature contour plot from a computational fluid dynamics (CFD) flowfield visualization of an RDE simulation. Fuel and oxidizer entering from the inlet is detonated at the shock

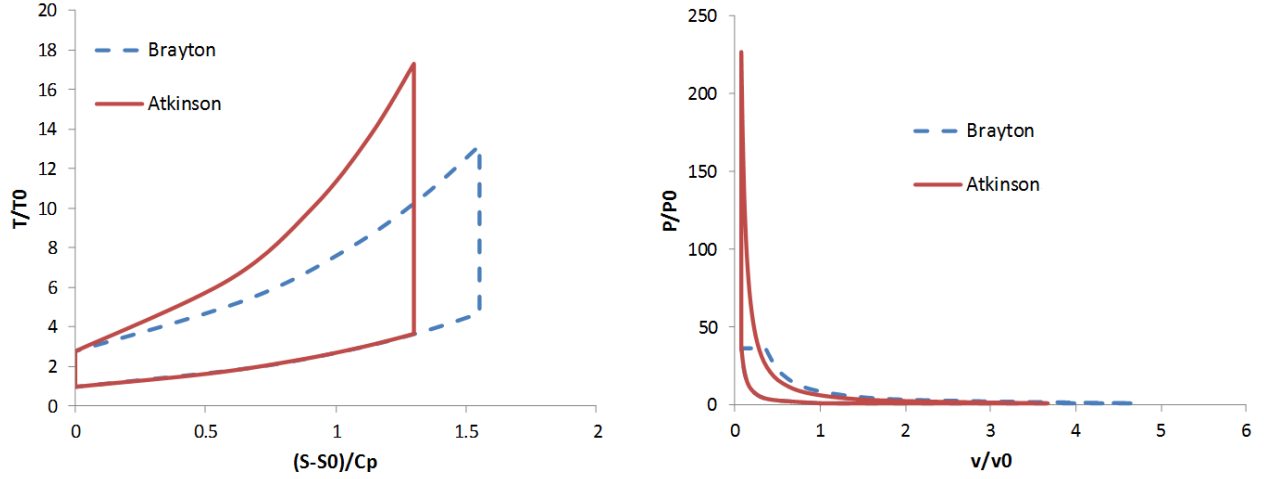


**Figure 1.** Comparison of thermodynamic diagrams for Brayton and Atkinson cycles [1]

wave traveling around the annulus and is expelled out of the exhaust end.

Since the radial thickness of the RDE is significantly smaller than the length or circumferential dimensions, radial variation is negligible [2–5; 10–14]. The three-dimensional RDE in Fig. 2 can be “unrolled” into the two-dimensional RDE in Fig. 3.

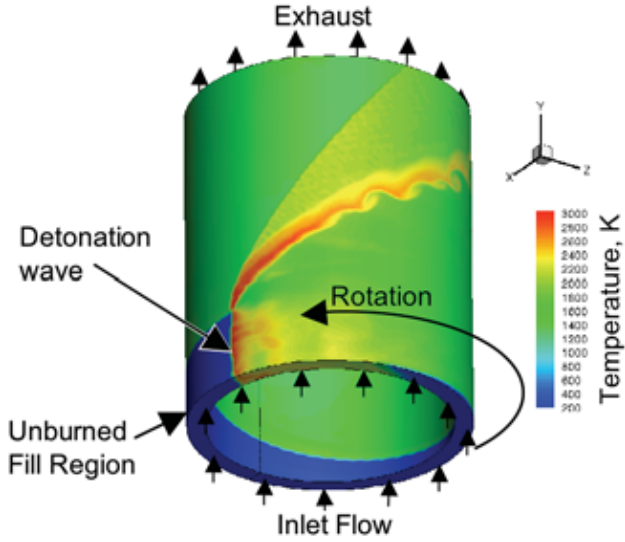


**Figure 2.** Temperature contour plot of an RDE simulation [2: Figure 1]

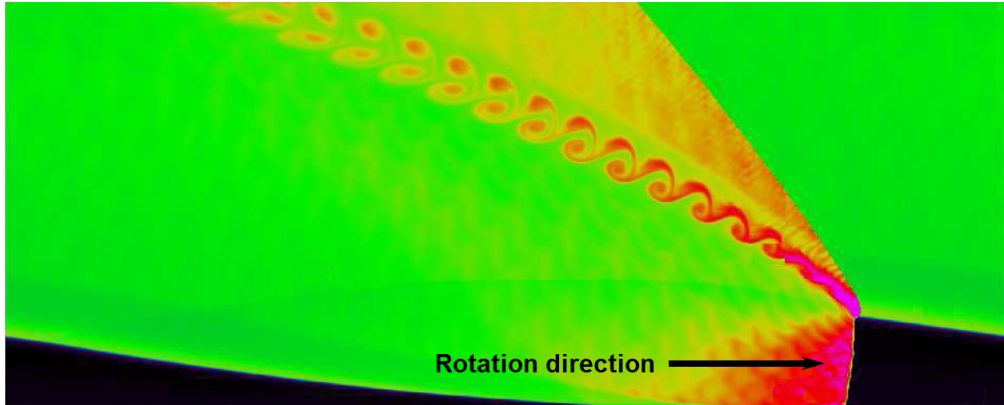


**Figure 3.** Two-dimensional “unwrapped” temperature contour plot of the RDE [3: Fig. 2]

## Problem

Kaemming developed a preliminary model of an RDE using Microsoft Excel and Microsoft Visual Basic macros [4]. The objective of this thesis was to develop a similar RDE model in Numerical Propulsion System Simulation (NPSS) and describe the utilization of the NPSS model in a rocket configuration. The rocket configuration consists of a flow inlet, the RDE, and the exhaust.

## Methodology

The first step in the analysis of the RDE is the translation of the RDE element based on the Kaemming model [4] into an NPSS element. The new NPSS element is incorporated into a full RDE model by initializing and attaching the air inlet, fuel inlet, and exhaust fluid ports. The results of running the NPSS model were compared to results from the Kaemming model [4; 15] and published CFD simulations [3; 14].

## II. Previous Work on Rotating Detonation Engines

This section describes the station numbering, a thermodynamic overview of the RDE, and the empirical models used in the RDE model.

### Station Designation

A station designation consistent with previously accepted station numbering designations has been agreed upon by Joint Army Navy National Aeronautics and Space Administration (NASA) Air Force (JANNAF) (in JANNAF-GL-2013-01) and Society of Automotive Engineers (SAE) (in SAE AS755f) [15; 16], illustrated in Fig. 4. In the rocket configuration implemented in this thesis, the inlet exit, air valve exit, and RDE entrance are assumed to be collocated (*i.e.*, station 3 is the same as 3\*).

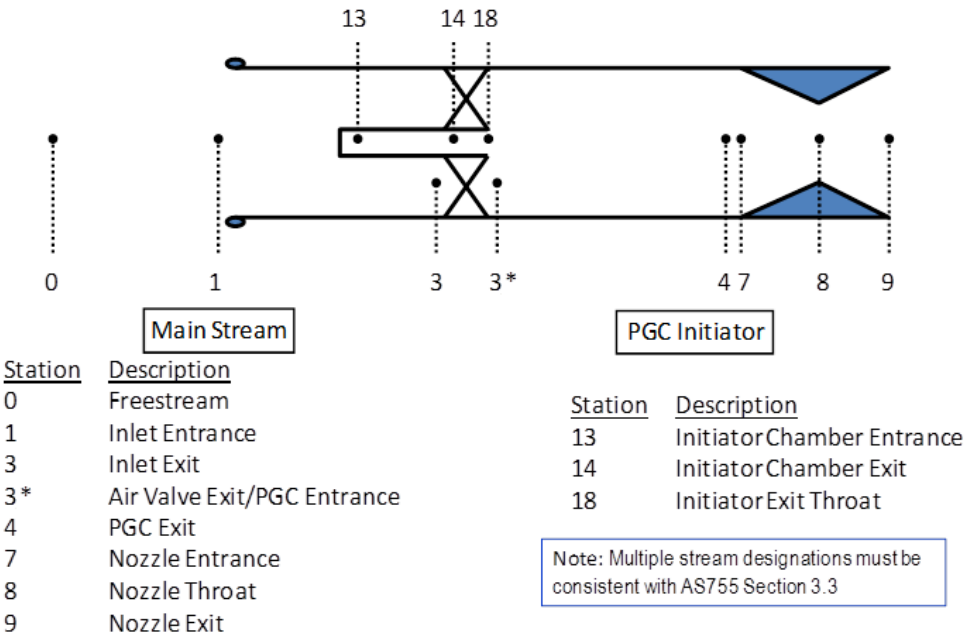
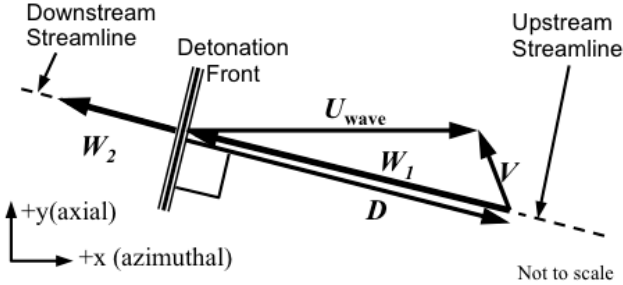


Figure 4. Station designations used in rocket configuration[4: Fig. 3-1]

## Thermodynamic Overview

There has been considerable thermodynamic analysis of the RDE [2; 5; 11; 13], so only a summary is provided here. The main process taking place in the RDE is the detonation wave. A steady-state, one-directional planar detonation can be modeled based on Zel'dovich, von Neumann, and Döring (ZND) theory [2; 5; 11; 13]. In the “unrolled” RDE, the detonation wave is a traveling planar wave, so the traditional ZND model does not apply in its present state [2; 11; 13].

Nordeen [11] modified the ZND model using velocity triangles to change the frame of reference from the laboratory frame-of-reference to the detonation wave frame-of-reference. A graphical representation of a velocity triangle is illustrated in Fig. 5. In Fig. 5,  $U_{wave}$  is the azimuthal wave speed traveling to the right in the laboratory frame-of-reference and  $V$  is the time-averaged velocity of the main flow [5]. The normal velocities of the flow upstream and downstream of the detonation front are given by  $W_1$  and  $W_2$ , respectively [5]. In Fig. 5,  $D$  is the normal speed of the detonation wave in the laboratory frame-of-reference, and is equal and opposite to  $W_1$  [5]. In the detonation wave frame-of-reference, the flow appears steady and the ZND theory can be applied [5; 11].



**Figure 5. Velocity triangles used to change between laboratory frame-of-reference and detonation wave frame-of-reference [5: Fig. 5]**

Schwer and Kailasanath tracked the paths of fluid particles through a CFD simulation of the RDE in the detonation frame-of-reference [3]. Schwer and Kailasanath defined three distinct thermal regions in the solution: Detonation-A (detonation followed by an oblique

shock wave), Detonation-B (detonation only), and Non-detonation (deflagration) [3]. The pathlines and three thermal regions are illustrated in Fig. 6.

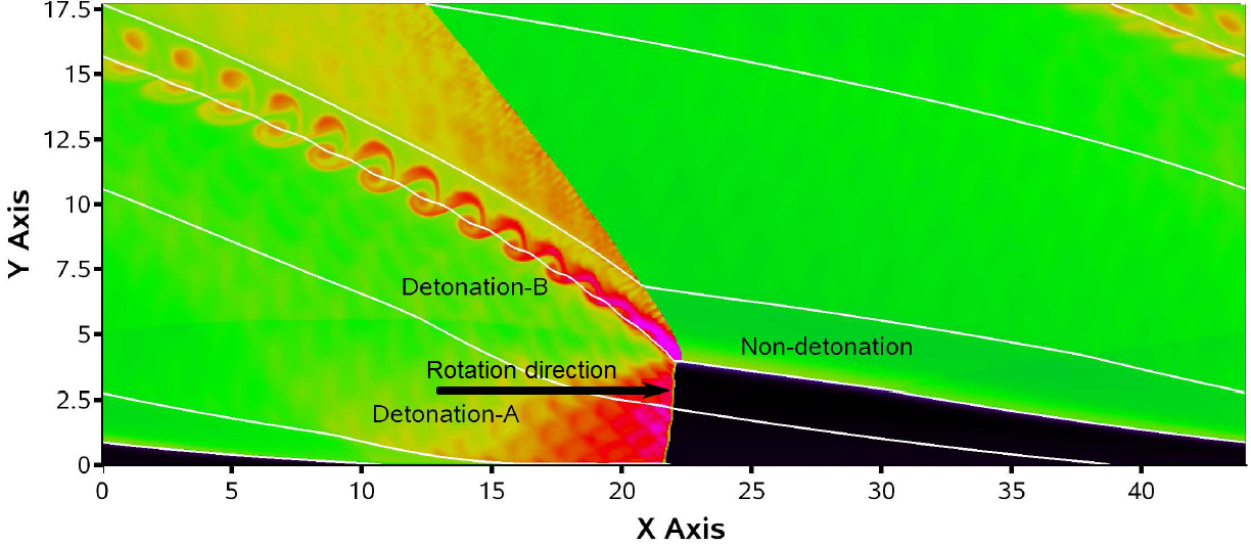


**Figure 6. Two-dimensional “unrolled” RDE with tracked pathlines and three thermal regions [3: Fig. 8]**

Kaemming extended the results from Schwer and Kailasanath [3] with the introduction of a mixed region [4]. Additionally, Kaemming added substation nomenclature to organize each of the steps along each of the regions. Kaemming’s [4] nomenclature is illustrated in Fig. 7. The letters *a–d* describe the paths through the thermal regions: path *a* has only detonation, path *b* has detonation followed by an oblique shock, path *c* has deflagration, and path *d* has a mixture of paths *a*, *b*, and *c* [4].

The air and fuel enter the RDE at station 3\* and are injected into the flow to substation 3.2. Substation 3.2 properties apply to all flow prior to combustion, and all of the paths pass through it [4]. Table 4 summarizes the processes that take place between substations. The flow traveling along paths *a* and *b* pass through a detonation between substation 3.2 and *a*3.4 and *b*3.4, respectively [4]. The flow traveling along path *a* continues to travel to the exit of the RDE. The flow traveling along path *b* passes through an oblique shock between substations *b*3.4 and *b*3.6, and then continues to travel to the exit of the RDE [4].

The flow traveling along path *c* is deflagrated between substations 3.2 and *c*3.4, and then passes through an oblique shock between substations *c*3.4 and *c*3.6[4]. All of the flow at substation *c*3.6 mixes with portions of the flow from substations *a*3.4 and *b*3.6; the mixed flow is substation *d*3.6. The percentage of the flows from substations *a*3.4 and *b*3.6 entering the mixed region is dictated by empirical models [4]. The three remaining paths *a*3.4, *b*3.6, and *d*3.6 travel to their respective substation exits: *a*4, *b*4, and *d*4. The RDE exit station 4 is a combination of the substation exits *a*4, *b*4, and *d*4.

The analysis of each path is described in Chapter III.

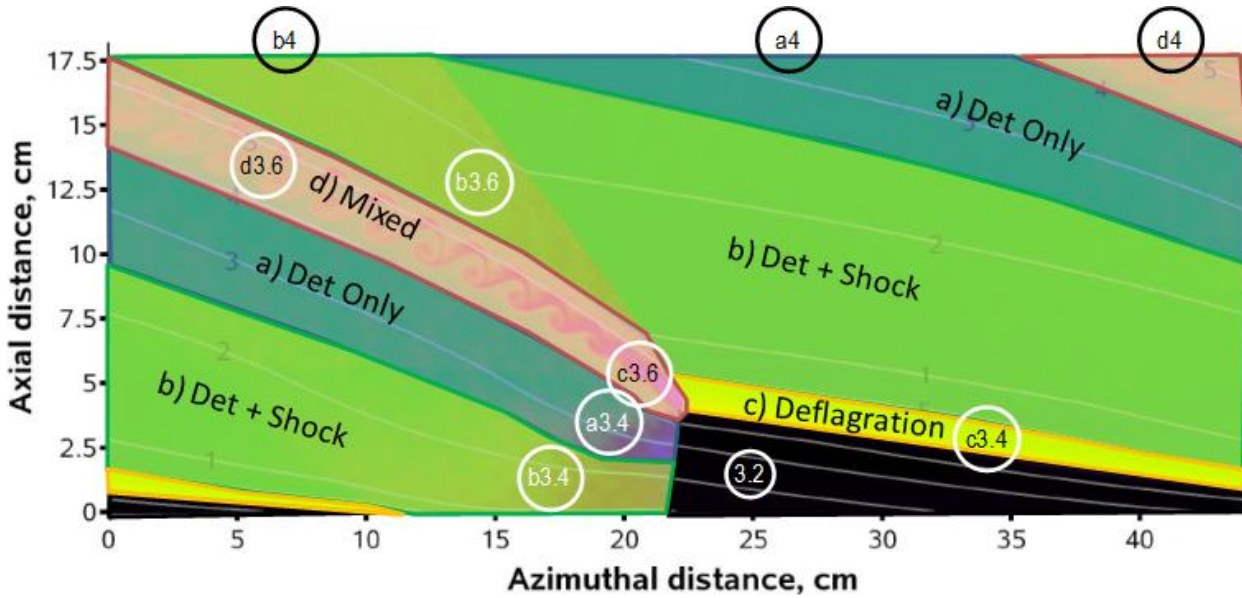


Figure 7. Path and substation nomenclature [4: Fig. 7-2]

**Table 4. Description of particle movement between substations**

From	To	Process
3*	3.2	Air and fuel injected into RDE
	a3.4	Detonation
	b3.4	Detonation
	c3.4	Deflagration
b3.4	b3.6	Oblique shock
c3.4	c3.6	Oblique shock
a3.4 (partial) b3.6 (partial) c3.6 (all)	d3.6	Mixing based on empirical models
a3.4 (remaining)	a4	Exit RDE
b3.6 (remaining)	b4	Exit RDE
d3.6 (all)	d4	Exit RDE

## Empirical Models

Kaemming developed several empirical models based on CFD simulations to reduce the overall complexity of the solution procedure [3; 4; 14]. The models are discussed below.

### Plenum Model.

CFD simulations [3; 14] show that the rotation of the detonation wave around the annulus of the RDE causes a variation of static pressure  $P_{3.2}$  at the air and fuel injectors [3; 14]. The thermodynamic properties of the remainder of the RDE depend on  $P_{3.2}$ , so a model was required to account for this variation along the plenum. Kaemming developed the empirical model seen in Eq. 1 and Eq. 2 for the injector pressure profile based on the results from CFD simulations [3; 4; 14]. The value of  $P_{3.2}$  varies with azimuthal location, but is based on the maximum value of  $P_{3.2}(0)$ , which is the value of  $P_{3.2}$  used in the current iteration ( $P_{3.2}$  is further described in Chapter III). In Eq. 1, the term  $b$  is the fractional pressure drop and  $\tau_{drop}$  is the time until the first drop [4]. In Eq. 2, the term  $\left(\frac{P_{3.4}}{P_{3.2}}\right)_{det}$  is the

ratio of static pressures after and before the detonation.

$$k = -\frac{\ln(1-b)}{\tau_{drop}} \quad (1)$$

$$P_{3.2}(t) = P_{3.2}(0) \left\{ 1 + \left[ \left( \frac{P_{3.4}}{P_{3.2}} \right)_{det} - 1 \right] e^{-kt} \right\} \quad (2)$$

Published results[3] showed the pressure profile as a function of azimuthal location, while the empirical model in Eq. 1 and Eq. 2 showed pressure profile as a function of time [4]. Kaemming used the detonation velocity to convert the time to distance, and the RDE circumference to convert the azimuthal distance to azimuthal location [15]. The final profile was translated by  $180^\circ$  and the pressure was converted from pounds per square inch to atmospheres to match the CFD results. Kaemming found that  $b = 0.80$  and  $\tau_{drop} = 0.00005$  sec produced a pressure profile most closely matching CFD results [4].

The empirical models from Eq. 1 and Eq. 2 are used in the NPSS model. A comparison of the pressure profiles at station 3.2 in the Kaemming and NPSS models to the profile found from the CFD simulations is illustrated in Fig. 8. The pressure profile example in Fig. 8 is based on a specific case using the same input parameters as CFD simulations, summarized in Table 6. Overall, the simple model follows the CFD results closely; however, two regions of significant deviation can be seen at azimuthal locations of  $85^\circ$  and  $165^\circ$ . Kaemming claims the deviations are the result of second-order effects, such as secondary waves, that may affect operation of a real RDE, but do not affect performance analysis [4]. The agreement of the Kaemming model with CFD simulations support the claim [3; 14].

### **Detonation Height Ratio Empirical Models.**

Kaemming developed several empirical models that are functions of the ratio of the calculated detonation height to the user-defined RDE height  $\left(\frac{h_{det}}{h_{RDE}}\right)$  [4]. Kaemming developed the empirical models by simplifying CFD solutions and profiles [4; 15]. The non-dimensional

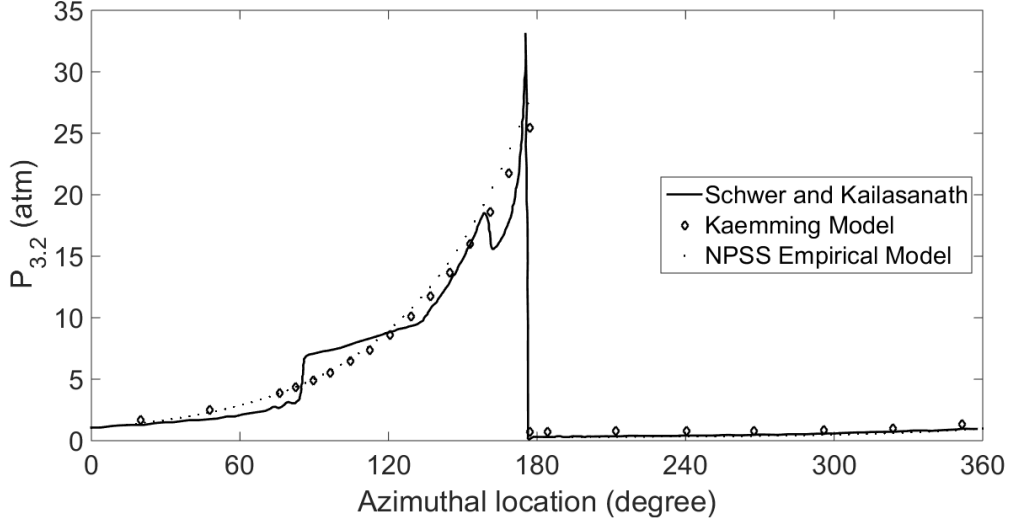


**Figure 8.** Comparison of pressure profile from CFD results to model from Eq. 1 and Eq. 2 [4: Fig. 6-1; 3: Fig. 9]

ratio of heights allows the RDE model to be scaled; however, experimental comparisons have not been accomplished to determine the accuracy of the scaling.

In the NPSS model, the empirical models are implemented in the form of tables, where the program calculates the value of  $\frac{h_{det}}{h_{RDE}}$  and interpolates within the models shown in Fig. 9.

The “Detonation Plus Shock Flow Fraction” model in Fig. 9 provides the fraction of the total detonated flow entering the oblique shock [4]. The model is mathematically described in Eq. 3.

$$\text{Detonation Plus Shock Flow Fraction} = \frac{\dot{m}_{\text{path } b}}{\dot{m}_{\text{path } a} + \dot{m}_{\text{path } b}} \quad (3)$$

The value returned from Fig. 9 provides the percentage of detonated flow that follows path *b*. The remainder of the flow follows path *a*.

The “Relative Mixing” model in Fig. 9 provides the relative amount of detonated flow that mixes with the deflagrated flow [4]. The model is mathematically described in Eq. 4.

$$\text{Relative Mixing} = \frac{\dot{m}_{\text{detonated flow mixing with path } d}}{\dot{m}_{\text{path } c}} \quad (4)$$

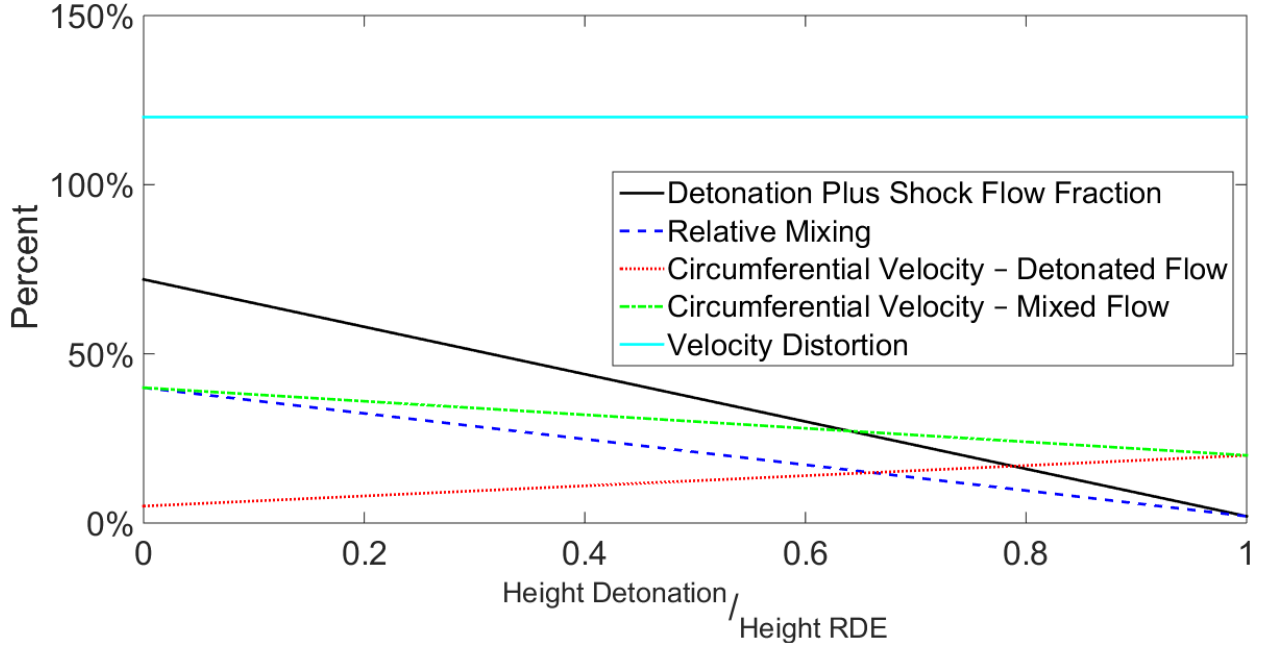


**Figure 9. Empirical models based on the ratio of detonation height to RDE height**

The value returned from Fig. 9 provides the ratio of mixed detonated flow to total deflagrated flow from path *c*. Kaemming approximates that half of the detonated flow entering the mixing region is from path *a* and the other half from path *b* [4]. All of the deflagrated flow from path *c* enters the mixing region, so the total mass flow entering path *d* is given by Eq. 5.

$$\dot{m}_{\text{path } d} = \dot{m}_{\text{detonated flow mixing into path } d} + \dot{m}_{\text{path } c} = \dot{m}_{\text{path } c} (1 + \text{Relative Mixing}) \quad (5)$$

The “Circumferential Velocity - Detonated Flow” and “Circumferential Velocity - Mixed Flow” models in Fig. 9 provide the mass-averaged circumferential (azimuthal) velocity for the detonated and mixed flows relative to the total velocity of the detonated or mixed flows, respectively. The “Circumferential Velocity - Detonated Flow” and “Circumferential Velocity - Mixed Flow” models are mathematically described in Eq. 6 and Eq. 7, respectively.

$$\text{Circumferential Velocity - Detonated Flow} = \frac{\dot{m}_{\text{detonated,circumferential}}}{\dot{m}_{\text{detonated,axial}} + \dot{m}_{\text{detonated,circumferential}}} \quad (6)$$

$$\text{Circumferential Velocity - Mixed Flow} = \frac{\dot{m}_{mixed,circumferential}}{\dot{m}_{mixed,axial} + \dot{m}_{mixed,circumferential}} \quad (7)$$

The percentage of circumferential velocity for the detonated flow increases with non-dimensionalized detonation height, as seen in Fig. 9. A higher proportion of  $\frac{h_{det}}{h_{RDE}}$  means the detonation takes up more of the RDE chamber, and, conversely, the non-detonated flow takes up less of the RDE chamber. The shock waves try to align the exiting flows, and the smaller non-detonation region causes a greater percentage of the flow to travel in the circumferential direction [4]. Conversely, with the mixed flow, the percentage of rotating flow decreases as the detonation height increases because the flow mixes in a smaller region, requiring less rotation [4].

The flow exiting the RDE is highly irregular [3; 4; 14; 17]. The “Velocity Distortion” model in Fig. 9 characterizes the exit velocity using the maximum, minimum, and mass-averaged velocities mathematically described in Eq. 8 [4]. The Kaemming and NPSS models both use a constant velocity distortion of 120% [4] based on exit velocity profiles found from CFD simulations [14].

$$\text{Velocity Distortion} = \frac{V_{max} - V_{min}}{V_{avg}} \quad (8)$$

Kaemming also found that the exit mass flows in the CFD solutions [3; 14] have the same corrected mass flow [15]. In the Kaemming model, the exit flow is assumed to be choked [4]. However, the choked flow assumption calculates an exit mass flow and momentum flux higher than the actual values because of the velocity distortion [15]. Kaemming uses correction terms for the mass ( $\frac{m}{m^*}$ ) and momentum ( $\frac{mV}{mV^*}$ ) based on variations in the velocity distortion [4]. The mass and momentum correction terms are mathematically described in Eq. 9 and Eq. 10, respectively, and are illustrated in Fig. 10 [4]. To find the actual exit flow, the correction terms are applied to the calculations where choked exit flow was assumed [15]. For the constant velocity distortion of 120%, the correction terms are treated as constants:

$\frac{m}{m^*} = 0.8555$  and  $\frac{mV}{mV^*} = 0.8682$ .

$$\frac{m}{m^*} = [-0.1004 \text{ (Velocity Distortion)} + 0.0001] \text{ (Velocity Distortion)} + 1 \quad (9)$$

$$\frac{mV}{mV^*} = [-0.0918 \text{ (Velocity Distortion)} + 0.0003] \text{ (Velocity Distortion)} + 1 \quad (10)$$

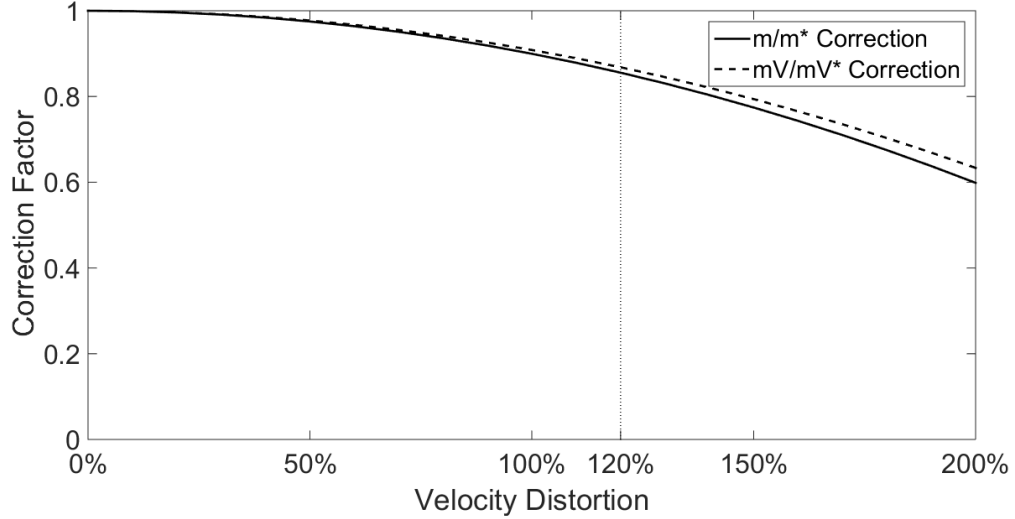


Figure 10. Correction factor for the mass ( $m/m^*$ ) and momentum ( $mV/mV^*$ )

## Summary

A station designation has been agreed upon by JANNAF and SAE that conforms to traditional engine station numbering. The thermodynamic analysis of all of the streamlines in the RDE is reduced to four paths. Several empirical models are used to simplify the complex flow interactions in the RDE.

### III. Model Summary

The NPSS RDE model is composed of four elements: the air source, the fuel source, the exhaust, and the RDE element itself. The flow into the RDE includes the air and fuel elements, while the exhaust element receives all of the exhaust from the RDE element. The air source, fuel source, and exhaust elements are all ideal components with no losses, as are all the ports that link these elements to the RDE element. In all cases, hydrogen fuel ( $H_2$ ) is used, though the current model allows for the use of ethylene ( $C_2H_4$ ).

The functions utilized to perform repeated calculations are summarized in Table 5. Detailed descriptions of these functions can be found in Appendix A.

**Table 5. Summary of functions implemented in RDE model**

Function	Description
PtqP	Isentropic pressure ratio
TtqT	Isentropic temperature ratio
M_PtqP	Calculate Mach number from isentropic pressure ratio
M_TtqT	Calculate Mach number from isentropic temperature ratio
AqAstar	Isentropic area ratio for choked flow in a nozzle
Msub_A	Calculate subsonic Mach number from isentropic area ratio
Msup_A	Calculate supersonic Mach number from isentropic area ratio
P2qP1ns	Calculate pressure ratio across normal shock
Pt2qPt1ns	Calculate total pressure ratio across normal shock
T2qT1ns	Calculate temperature ratio across normal shock
M2ns	Calculate Mach number across normal shock
find_flow	Find mass flow to satisfy total area requirement for three separate streams
expansion_mode	Find exit Mach number for expanding flow from throat to exit
CJ_mach_area	Calculate Chapman-Jouguet Mach number with area relief
OneDNtrp	Interpolate along arrays

### RDE Element Summary

The Kaemming model is divided into three solution stages: entrance flow, thermodynamic analysis, and exit flow [4]. The NPSS RDE element closely follows the methodology of the

Kaemming model. The individual total pressure of the air ( $P_{t3,air}$ ) and fuel ( $P_{t3,fuel}$ ) entering the RDE element are known, but the pressure of the air and fuel mixture injected into the RDE (i.e.,  $P_{t3}$ ) is unknown. The RDE element iterates  $P_{3.2}$  until the calculated mass flow entering the RDE matches the calculated mass flow exiting the RDE. Figure 11 summarizes the implementation of the Kaemming model.

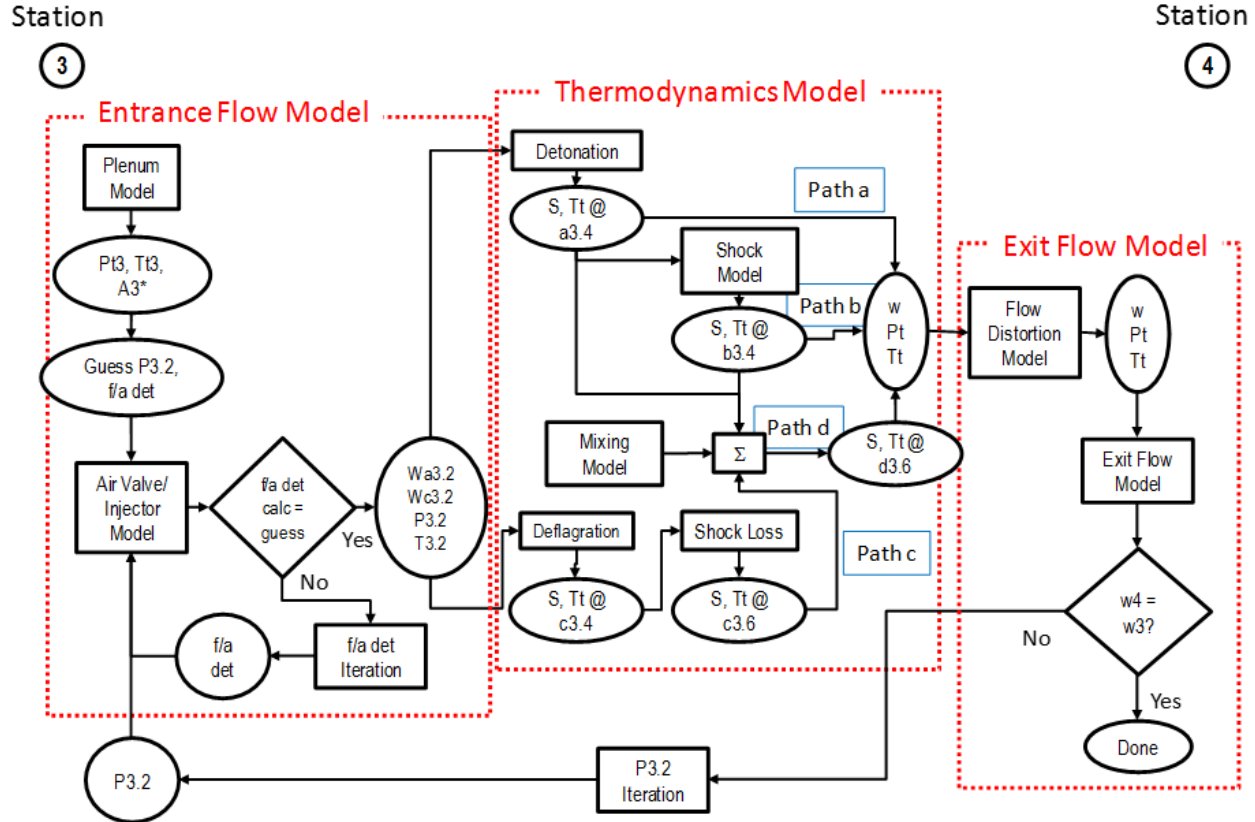


Figure 11. Summary of RDE element implementation [4: Fig. 5-1]

The default parameters and values for user-defined inputs to the RDE element are summarized in Table 6. Table 6 also summarizes the mathematical and NPSS variable names of the parameters. These parameter values must be changed in the element code itself, not the run file. The values for the parameters in Table 6 are based on RDE geometry, model test conditions, or from Kaemming's analysis of CFD simulations [3; 4; 14].

Since the flow direction is assumed to be two-dimensional, an  $xy$ -coordinate system is

used. The  $x$ -direction is the circumferential or azimuthal direction, while the  $y$ -direction is the axial direction from the inlet to exhaust. In several cases, different frames-of-reference are implemented. Static thermodynamic properties are independent of the frame-of-reference, while total thermodynamic properties and relative velocities are affected by the frame-of-reference. Variables used for analysis in the laboratory frame-of-reference do not have any additional subscripts. Variables used for analysis in the detonation wave frame-of-reference have the subscript  $w$ .

**Table 6. Default values for user-defined input parameters**

Parameter Description	Math Variable	Code Variable	Default Value
Mean RDE throughflow diameter	$D_m$	<code>D_m</code>	140 mm
RDE thickness	$\tau$	<code>tau</code>	10 mm
RDE height	$h_{RDE}$	<code>Ht</code>	177 mm
Total pressure entering RDE	$P_{t3,air}$	<code>Pt3_air</code>	58.784 psia
	$P_{t3,fuel}$	<code>Pt3_fuel</code>	58.784 psia
Total temperature entering RDE	$T_{t3,air}$	<code>Tt3_air</code>	540 R
	$T_{t3,fuel}$	<code>Tt3_fuel</code>	540 R
Oblique shock angle relative to flow	$\theta_{shock}$	<code>theta_shock</code>	60°
Number of detonation waves	$n_{waves}$	<code>n_wave</code>	1
Deflagration flame speed at standard conditions	$V_{defl,std}$	<code>V_flame</code>	10 ft/s
Injector-to-throat area ratio	$\frac{A_{inj,air}}{A_3}$	<code>AinjqA3_air</code>	0.1801
	$\frac{A_{inj,fuel}}{A_3}$	<code>AinjqA3_fuel</code>	0.0199
Station 3 flow coefficient	$C_{W3,fwd,air}$	<code>cw_fwd_air</code>	1
	$C_{W3,bwd,air}$	<code>cw_back_air</code>	0
	$C_{W3,fwd,fuel}$	<code>cw_fwd_fuel</code>	1
	$C_{W3,bwd,fuel}$	<code>cw_back_fuel</code>	0
Ambient pressure	$P_0$	<code>P0</code>	14.7 psia
Combustion chamber area contraction	$\frac{A_8}{A_3}$	<code>A8qA3</code>	1
RDE exit flow coefficient	$C_{W8}$	<code>Cw8</code>	1
Nozzle area ratio	$\frac{A_9}{A_8}$	<code>A9qA8</code>	1
Nozzle stream thrust coefficient	$C_S$	<code>Cs</code>	1
Axial Mach number at throat, path a	$M_{a8y}$	<code>M8y_det</code>	1
Axial Mach number at throat, path b	$M_{b8y}$	<code>M8y_det_shk</code>	1
Axial Mach number at throat, path d	$M_{d8y}$	<code>M8y_mix</code>	1
Detonation lateral area relief	$\left(\frac{A_{3.4}}{A_{3.2}}\right)_{CJ}$	<code>A2qA1_CJ</code>	1

## Initial Calculations

Before the NPSS model implements the Kaemming model illustrated in Fig. 11, several parameters are calculated based on the input conditions from Table 6. In the Kaemming model, these parameters are automatically calculated (based on the input parameters) because Microsoft Excel automatically updates linked cells; however, NPSS does not automatically update linked cells, so the values must be manually updated.

### Geometric Parameters.

The first group of calculations are for geometric parameters. The inner and outer diameters are calculated using Eq. 11 and Eq. 12, respectively. The effective circumference per detonation wave is calculated using the mean diameter from Eq. 13. The cross-section through-flow area per detonation wave is calculated using Eq. 14. The air and fuel injector areas are calculated by multiplying  $A_3$  by the ratios  $\frac{A_{inj,air}}{A_3}$  and  $\frac{A_{inj,fuel}}{A_3}$ , respectively, from Table 6. In the default case,  $n_{wave} = 1$ .

$$D_i = D_m - \tau \quad (11)$$

$$D_o = D_m + \tau \quad (12)$$

$$C_{eff} = \frac{\pi D_m}{n_{wave}} \quad (13)$$

$$A_3 = \left(\frac{\pi}{4}\right) \left(\frac{D_o^2 - D_i^2}{n_{wave}}\right) \quad (14)$$

### Gas Properties for Input to NPSS.

The second group of calculations are for gas properties. In the NPSS model, gas properties are calculated based on two variables: `fuel` and `gas_prop_flag`. The `fuel` parameter indicates the fuel used, either hydrogen  $H_2$  or ethylene  $C_2H_4$ . Table 7 summarizes the gas properties for

the air, hydrogen, and ethylene. Gas properties for the fuel and air reactants as well as the post-detonation mixed products are calculated ahead of time outside of the NPSS model using either known values or the NASA computer program Chemical Equilibrium with Applications (CEA).

The variable `gas_prop_flag` determines if the gas properties for the reactants are taken from a lookup table or calculated [4]. Kaemming used the tabulated lookup values summarized in Table 8 for hydrogen from CFD simulations [3; 14] and for ethylene from CEA [4; 15].

**Table 7. Gas properties for air, hydrogen, and ethylene**

Parameter	Air	Hydrogen	Ethylene
Molecular weight, $MW$ ( $kg/kmol$ )	28.965	2.016	28.05
Ratio of specific heats, $\gamma$	1.400	1.405	1.2313
Specific gas constant, $R \left( \frac{J}{kg-K} \right)$	287.052	4124.236	296.416
Stoichiometric fuel-to-air ratio, $FAR_{stoich}$	–	0.0292	0.0676
Heat of combustion, $\Delta H \left( \frac{kJ}{kg-K} \right)$	–	3550	3181

**Table 8. Tabulated gas properties for reactants**

Parameter	Hydrogen	Ethylene
Ratio of specific heats, $\gamma_R$	1.4256	1.3690
Specific gas constant, $R_R \left( \frac{J}{kg-K} \right)$	397.500	288.807

Kaemming calculates the reactant properties using the inlet conditions from Table 6 to find the fuel-to-air ratio at the detonation and then mole-averages the gas properties from Table 7 [4]. Kaemming assumed the injectors are choked, so the mass flow parameter for the air and fuel are calculated using Eq. 15 and Eq. 16, respectively [7].

$$MFP_{air} = \sqrt{\frac{\gamma_{air} g_c}{R_{air}}} \left( 1 + \frac{\gamma_{air} - 1}{2} \right)^{\left[ \frac{\gamma_{air} + 1}{2(1-\gamma_{air})} \right]} \quad (15)$$

$$MFP_{fuel} = \sqrt{\frac{\gamma_{fuel} g_c}{R_{fuel}}} \left( 1 + \frac{\gamma_{fuel} - 1}{2} \right)^{\left[ \frac{\gamma_{fuel} + 1}{2(1-\gamma_{fuel})} \right]} \quad (16)$$

The mass flow parameter is related to the mass flow by Eq. 17 [7: Eq. 1.3]. The detonation fuel-to-air ratio was calculated as a ratio of the fuel mass flow rate to the air mass flow rate using Eq. 18.

$$\dot{m} = \left( \frac{P_t A}{\sqrt{T_t}} \right) (MFP) \quad (17)$$

$$FAR_{det} = \frac{\dot{m}_{fuel}}{\dot{m}_{air}} = \left( \frac{P_{t3,fuel}}{P_{t3,air}} \right) \left( \frac{A_{inj,fuel}}{A_{inj,air}} \right) \left( \frac{MFP_{fuel}}{MFP_{air}} \right) \sqrt{\frac{T_{t3,air}}{T_{t3,fuel}}} \quad (18)$$

The mole fraction for a species  $i$  is defined using Eq. 19 [18].

$$X_i = \frac{\frac{m_i}{MW_i}}{\sum_i \frac{m_i}{MW_i}} \quad (19)$$

The fuel-to-air ratio is used to calculate the mole fraction for air and fuel using Eq. 20 and Eq. 21, respectively.

$$X_{air} = \left( \frac{1}{MW_{air}} \right) \left( \frac{1}{\frac{1}{MW_{air}} + \frac{FAR_{det}}{MW_{fuel}}} \right) \quad (20)$$

$$X_{fuel} = \left( \frac{FAR_{det}}{MW_{fuel}} \right) \left( \frac{1}{\frac{1}{MW_{air}} + \frac{FAR_{det}}{MW_{fuel}}} \right) \quad (21)$$

Kaemming uses the mole fractions to take a weighted average of the molecular weight and ratio of specific heats using Eq. 22 and Eq. 23, respectively [4; 19].

$$MW_R = MW_{air}X_{air} + MW_{fuel}X_{fuel} \quad (22)$$

$$\gamma_R = \gamma_{air}X_{air} + \gamma_{fuel}X_{fuel} \quad (23)$$

The molecular weight is used to calculate the specific gas constant using Eq. 24.

$$R_R = \frac{R_U}{MW_R} \quad (24)$$

In both the tabular lookup (Table 7 and Table 8) and calculated cases (Eqs. 15–24), the gas properties for the products are taken from a lookup table based on CEA results [4; 15]. Kaemming

uses fixed values for the products because the properties cannot be calculated *a priori* [4; 15]. The assumption of constant  $R_P$  and  $\gamma_P$  is a valid approximation to actual properties, even with variations in pressure and temperature [2]. Table 9 summarizes the values used for the products.

**Table 9. Tabulated gas properties for products**

Parameter	Hydrogen	Ethylene
Ratio of specific heats, $\gamma_P$	1.2412	1.2300
Specific gas constant, $R_P \left( \frac{J}{kg-K} \right)$	347.700	298.191

## Entrance Flow Model

In the NPSS model, the subroutine `iter8` initializes the iteration for the pressure at station 3.2 and ensures the fuel-to-air ratios are appropriately updated. Both the Kaemming and NPSS models assume separate injectors for the air and fuel streams; the parameters  $\frac{A_{inj,air}}{A_3}$  and  $\frac{A_{inj,fuel}}{A_3}$  from Table 6 describe the proportion of the total area made up of air or fuel injectors, respectively [4]. Additionally, both models allow for forward (injection) and backward (blowback) flow for the air or fuel injectors [4]; the station three flow coefficients ( $C_{W3}$ ) from Table 6 govern the forward or backward direction of flow for the air and fuel. In the default setup, all flow is assumed to be forward flow ( $C_{w3,fwd} = 1$ ) with no backflow ( $C_{w3,bwd} = 0$ ) [4].

Kaemming finds a minimum value of  $P_{3.2}$  based on isentropic expansion from the injector into the RDE chamber (i.e., station 3\* to substation 3.2) [4]. The amount of expansion is based on the total area of injectors and the total area in the RDE chamber, given by Eq. 25. The expansion is multiplied by the mass-averaged forward mass flow coefficient, given by Eq. 26.

$$\frac{A_3}{A_{inj,total}} = \frac{1}{\frac{A_{inj,air}}{A_3} + \frac{A_{inj,fuel}}{A_3}} \quad (25)$$

$$C_{W3,fwd,eff} = \frac{C_{W3,fwd,air} + FAR_{det}C_{W3,fwd,fuel}}{1 + FAR_{det}} \quad (26)$$

The maximum Mach number associated with the area expansion  $\frac{A_3}{A_{inj,total}}$  is found using the function

**Table 10.** Grid convergence study for discretized entrance flow model with percent change based on 100-step solution

Steps	Time (sec)	Specific Impulse (sec)	% Change
50	3	2922.28	1.6%
100	4	2970.43	–
200	6.5	2986.29	-0.53%

`Msup_A`. The Mach number is used to find the minimum pressure at station 3.2 using the function `PtqP` and the total pressure  $P_{t3}$  entering the RDE from Table 6.

The entrance flow model calculates the thermodynamic properties of the flow entering the RDE, as seen in Fig. 11 [4]. In the NPSS element, the entrance flow model calculations are performed in the `fill_calc` subroutine. The duration of each cycle is calculated using Eq. 27 [4]. The calculation of the detonation velocity  $V_{det}$  is described later.

$$t_{cycle} = \frac{C_{eff}}{V_{det}} \quad (27)$$

Each cycle is discretized into 100 steps. Table 10 summarizes a grid convergence study showing the number of discretized steps, time to complete the entire solution, calculated specific impulse, and percent change from the 100-step solution. The specific impulse calculation used the default input values from Table 6. In all three cases summarized in Table 10, the specific impulse does not significantly change, suggesting that the solution has reached a stable solution. The use of 100 steps provides a balance of solution precision and computational time.

The `fill_calc` subroutine uses  $P_{3.2}$  from the `iter8` subroutine in the empirical plenum model from Eq. 1 and Eq. 2 to model the pressure profile inside the combustion chamber [4]. The modeled pressure determines if the flow is moving forwards or backwards by comparing the modeled pressure to the pressure of the air and fuel from Table 6 [4]. The direction of the flow dictates an increase or decrease in air or fuel, and the amount of air or fuel mass flow is calculated using Eq. 28 with the appropriate values based on Table 11. The mass flow rate is multiplied by the length of the discretized time step to calculate the mass of the air and fuel used. The injection Mach number

$M_{inj}$  has an upper limit of one for the choked condition [4]. The properties at substation 3.4 are calculated outside of the `fill_calc` subroutine and is described later.

$$\dot{m} = C_W P A M \sqrt{\frac{\gamma g_c}{RT}} \quad (28)$$

**Table 11. Parameters used in air and fuel fill calculations based direction of flow using values from Table 6**

	<b>Forward</b>	<b>Backward</b>
<b>Air</b>	$C_W = C_{W,fwd,air}$ $M = f(P_{t3,air}/P_{3.4})$ $P = f(P_{t3,air}, M)$ $T_{t,air} = T_{t3,air}$ $T = f(T_{t3,air}, M)$ $A = A_{inj,air}$ $\gamma = \gamma_{air}$ $MW = MW_{air}$ $R = \frac{R_U}{MW_{air}}$	$C_W = C_{W,bwd,air}$ $M = f(P_{3.4}/P_{t3,air})$ $P = f(P_3, M)$ $T_{t,air} = T_{t,a3.4}$ $T = f(T_{t,a3.4}, M)$ $A = A_{inj,air}$ $\gamma = \gamma_P$ $MW = MW_P$ $R = \frac{R_U}{MW_P}$
<b>Fuel</b>	$C_W = C_{W,fwd,fuel}$ $M = f(P_{t3,fuel}/P_{3.4})$ $P = f(P_{t3,fuel}, M)$ $T_{t,fuel} = T_{t3,fuel}$ $T = f(T_{t3,fuel}, M)$ $A = A_{inj,fuel}$ $\gamma = \gamma_{fuel}$ $MW = MW_{fuel}$ $R = \frac{R_U}{MW_{fuel}}$	$C_W = C_{W,bwd,fuel}$ $M = f(P_{3.4}/P_{t3,fuel})$ $P = f(P_3, M)$ $T_{t,fuel} = T_{t,a3.4}$ $T = f(T_{t,a3.4}, M)$ $A = A_{inj,fuel}$ $\gamma = \gamma_P$ $MW = MW_P$ $R = \frac{R_U}{MW_P}$

The `fill_calc` subroutine tracks masses of the air and fuel throughout each iteration. The tracked masses of air and fuel are used to calculate the total temperature, ratio of specific heats, and molecular weight of the mixture using mass-averaging based on Eqs. 29– Eq. 31, respectively, using values from Table 6 and Table 11 [4; 14].

$$T_{t,3.2} = \frac{\dot{m}_{air} T_{t,air} + \dot{m}_{fuel} T_{t,fuel}}{\dot{m}_{air} + \dot{m}_{fuel}} \quad (29)$$

$$\gamma_{3.2} = \frac{\left(\frac{\dot{m}_{air}}{MW_{air}}\right)\gamma_{air} + \left(\frac{\dot{m}_{fuel}}{MW_{fuel}}\right)\gamma_{fuel}}{\frac{\dot{m}_{air}}{MW_{air}} + \frac{\dot{m}_{fuel}}{MW_{fuel}}} \quad (30)$$

$$MW_{3.2} = \frac{\left(\frac{\dot{m}_{air}}{MW_{air}}\right)MW_{air} + \left(\frac{\dot{m}_{fuel}}{MW_{fuel}}\right)MW_{fuel}}{\frac{\dot{m}_{air}}{MW_{air}} + \frac{\dot{m}_{fuel}}{MW_{fuel}}} \quad (31)$$

The static pressure mass flow parameter definition is given in Eq. 32 [7: Eq. 1.4].

$$MFP = \frac{\dot{m}\sqrt{T_t}}{PA} = M\sqrt{\frac{\gamma g_c}{R} \left(1 + \frac{\gamma - 1}{2}M^2\right)} \quad (32)$$

Squaring Eq. 32 and rearranging the result leads to Eq. 33

$$\frac{\gamma - 1}{2} (M^2)^2 + M^2 + \left(\frac{\dot{m}}{PA}\right)^2 \left(\frac{RT_t}{\gamma g_c}\right) = 0 \quad (33)$$

The quadratic equation is used to find the the Mach number given in Eq. 34.

$$M = \sqrt{\frac{1}{2} \left[ \frac{-2}{\gamma - 1} + \sqrt{\left(\frac{2}{\gamma - 1}\right)^2 + 4 \left(\frac{\dot{m}}{PA}\right)^2 \left(\frac{2RT_t}{\gamma g_c(\gamma - 1)}\right)} \right]} \quad (34)$$

Kaemming uses Eq. 34 to calculate the Mach number at station 3.2, as seen in Eq. 35.

$$M_{3.2} = \sqrt{\frac{1}{2} \left[ \frac{-2}{\gamma_{3.2} - 1} + \sqrt{\left(\frac{2}{\gamma_{3.2} - 1}\right)^2 + 4 \left(\frac{\dot{m}_{air} + \dot{m}_{fuel}}{P_{3.2}A_3}\right)^2 \left(\frac{2\left(\frac{R_U}{MW_{3.2}}\right)T_{t,3.2}}{\gamma_{3.2}g_c(\gamma_{3.2} - 1)}\right)} \right]} \quad (35)$$

The total temperature and Mach number at station 3.2 are used to calculate the static temperature. The station 3.2 properties are used to calculate the velocity of the flow using Eq. 36 based on the definition of mass flow rate.

$$V_{3.2} = \frac{(\dot{m}_{air} + \dot{m}_{fuel})}{\left(\frac{P_{3.2}MW_{3.2}}{T_{3.2}R_U}\right)A_3} \quad (36)$$

Kaemming assumes the deflagration flame speed is proportional to density [20] based on Eq. 37.

The default flame speed of 10 *ft/sec* from Table 6 is at a standard pressure of  $P_{std} = 14.7 \text{ psia}$  and a standard temperature of  $T_{std} = 518.7 \text{ R}$  [4].

$$V_{flame,local} = V_{flame,std} \left( \frac{P}{P_{std}} \right) \left( \frac{T_{std}}{T} \right) \quad (37)$$

Kaemming tracks the deflagrated mass by comparing the local flame speed to  $V_{3.2}$ . If  $V_{3.2}$  is less than the local flame speed, all of the air and mass flow at the given time step is deflagrated [4]. If  $V_{3.2}$  is greater than the local flame speed, only a proportion of the air and mass flow is deflagrated based on Eq. 38 [4].

$$\Delta m_{defl} = (\dot{m}_{air} + \dot{m}_{fuel}) \Delta t \left( \frac{V_{3.2}}{V_{flame,local}} \right) \quad (38)$$

Additionally, Kaemming uses  $V_{3.2}$  to calculate the fill height of the flow during the cycle using Eq. 39 [4].

$$\Delta h_{fill} = V_{3.2} \Delta t \quad (39)$$

At each of the 100 steps, the `fill_calc` subroutine calculates and stores the following parameters in arrays: mass of air used, mass of fuel used, and fill height [4]. All three parameter arrays correspond to values in an array for the total mass, so the three parameter arrays can be seen as functions of the total mass. The `fill_calc` subroutine calculates the total mass of deflagrated products by summing the incremental calculations from Eq. 38 and uses the function `OneDNtrp` to interpolate along the total mass array and find corresponding values for the mass of air deflagrated, mass of fuel deflagrated, and deflagration fill height [4]. The percentage of the flow composed of deflagration is calculated by dividing the deflagration mass by the total mass at the end of the 100 steps, as seen in Eq. 40 [4]. The fuel-to-air ratio for the deflagrated flow is calculated using Eq. 41.

$$Z_{defl} = \left( \frac{m_{fuel,defl} + m_{air,defl}}{m_{tot}} \right) \quad (40)$$

$$FAR_{defl} = \frac{m_{fuel,defl}}{m_{air,defl}} \quad (41)$$

Kaemming assumes the remainder of flow not deflagrated is detonated [4]. The detonation

height is calculated by subtracting the deflagration height (previously found by interpolation) from the total fill height at the end of the 100 steps. The detonation height is divided by the height of the RDE to calculate the parameters from the empirical models from Fig. 9 and Fig. 10. The percent of the flow composed of detonation is calculated using Eq. 42. The detonation fuel-to-air ratio originally estimated in Eq. 18 is updated using Eq. 43.

$$Z_{det} = 1 - Z_{defl} \quad (42)$$

$$FAR_{det} = \frac{m_{fuel,tot} - m_{fuel,defl}}{m_{air,tot} - m_{air,defl}} \quad (43)$$

Kaemming calculates the average mass flow rate using Eq. 44. The average mass flow rate calculated in Eq. 44 is “w3” in Fig. 11.

$$\dot{m}_{3,avg} = \frac{m_{tot}}{t_{cycle}} \quad (44)$$

In the Kaemming model, the fill cycle calculations are used to update the air valve/injector model, as seen in Fig. 11 [4]. In the NPSS element, the subroutine `Inject_calcs` performs the air valve/injector model calculations. The fill cycle calculations are based on post-combustion properties while the air valve/injector model calculations are based on pre-combustion properties.

The injector Mach number  $M_{inj}$  for the air and fuel are calculated based on the ratio of their respective total pressures from Table 6 to the  $P_{3,2}$  for the current iteration. The air and fuel flow Mach numbers have an upper limit of one for choked flow. The Mach numbers are used to calculate the pressure  $P_{inj}$  and temperature  $T_{inj}$  of the air and fuel flows inside the injector. The Mach number, pressure, and temperature are used to calculate the mass flow for the air and fuel using Eq. 45 with the parameters from Table 12 [4]. Table 6 summarizes the default values for the parameters in Table 12.

$$\dot{m}_{inj} = C_W P_{AM} \sqrt{\frac{\gamma g_c}{RT}} \quad (45)$$

**Table 12. Parameters used for mass flow calculations**

Parameter	Air	Fuel
$C_W$	$C_{W3,fwd,air}$	$C_{W3,fwd,fuel}$
$P$	$P_{inj,air}$	$P_{inj,fuel}$
$A$	$A_{inj,air}$	$A_{inj,fuel}$
$M$	$M_{inj,air}$	$M_{inj,fuel}$
$\gamma$	$\gamma_{air}$	$\gamma_{fuel}$
$R$	$R_{air}$	$R_{fuel}$
$T$	$T_{inj,air}$	$T_{inj,fuel}$

The pressure and temperature streams are combined to get the mass-averaged total pressure and total temperature using Eq. 46 and Eq. 47, respectively [4].

$$P_{t3,sum} = \frac{P_{t3,air} + FAR_{det}P_{t3,fuel}}{1 + FAR_{det}} = P_{t3} \quad (46)$$

$$T_{t3,sum} = \frac{C_{P,air}T_{t3,air} + FAR_{det}C_{P,fuel}T_{t3,fuel}}{(1 + FAR_{det})C_{P,R}} = T_{t3} \quad (47)$$

Kaemming calculates the Mach number at station 3.2 based on the steady-state mass flow rate, static pressure, and total temperature using Eq. 48 [4]. The calculation for  $M_{3.2}$  in Eq. 35 is for a variable used internally in the `fill_calcs` subroutine.

$$M_{3.2} = \sqrt{\frac{1}{2} \left[ \frac{-2}{\gamma_R - 1} + \sqrt{\left( \frac{2}{\gamma_R - 1} \right)^2 + 4 \left( \frac{\dot{m}_{inj,air} + \dot{m}_{inj,fuel}}{P_{3.2}A_3} \right)^2 \left( \frac{2R_R T_{t3,sum}}{\gamma_R g_c (\gamma_R - 1)} \right)} \right]} \quad (48)$$

The Mach number and isentropic relations functions are used to calculate the station 3.2 total pressure  $P_{t,3.2}$  and static temperature  $T_{3.2}$  from  $P_{3.2}$  and  $T_{t3,sum}$ , respectively. The axial velocity at station 3.2 is calculated using Eq. 49 [4].

$$V_{3.2y} = M_{3.2} \sqrt{\gamma_R R g_c T_{3.2}} \quad (49)$$

## Thermodynamics Model

The exit flow model calculates the thermodynamic properties of the flow exiting the RDE, as seen in Fig. 11 [4]. In the NPSS element, the exit flow model calculations are performed in the `Thermo_parametric` subroutine. The exiting flow is composed of the four paths *a–d* in Fig. 7. Kaemming calculates the thermodynamic properties for the flow along each pathline to the exit of the RDE and then expands each stream to the exhaust based on throat Mach numbers defined in Table 6 [4]. After the properties for the separate streams are calculated all the way to ambient conditions, properties such as total temperature, specific thrust, and specific impulse are mass-averaged [4].

### Path *a*: Detonation Only.

The post-detonation (station *a3.4* in Fig. 7) properties are calculated using properties for the products and enthalpy addition. The total temperature at substation *a3.4* is calculated by assuming enthalpy addition to the station 3 properties based on Eq. 50 [4].

$$T_{t,a3.4} = \left( \frac{1}{C_{P,P}} \right) \left( C_{P,R} T_{t3,sum} + \frac{\Delta H}{1 + FAR_{det}} \right) \quad (50)$$

The non-dimensional heat addition term is calculated using Eq. 51 [4] (see Appendix A, Eqs. A.21–A.24). Substation 3.2 properties  $C_{P,R} T_{3.2}$  are used as the pre-detonation properties  $C_{P,1} T_1$  from Eq. A.24.

$$q = \frac{\Delta H (1 + FAR_{det})}{(C_{P,R} T_{3.2})} \quad (51)$$

The detonation Mach number  $M_{det}$  is calculated using the  $q$  term from Eq. 51 in the function `CJ_mach_area`. The detonation velocity is calculated using Eq. 52.

$$V_{det} = M_{det} \sqrt{\gamma_R g_c R_R T_{3.2}} \quad (52)$$

The pressure and temperature change across the detonation with lateral area relief are calculated using Eq. 53 and Eq. 54, respectively. By default, no lateral area relief is assumed (i.e.,  $\left(\frac{A_{3.4}}{A_{3.2}}\right)_{CJ} = 1$ ); further research is required to find appropriate values for  $\left(\frac{A_{3.4}}{A_{3.2}}\right)_{CJ}$ .

$$P_{a3.4} = P_{3.2} \left[ \frac{\gamma_R M_{det}^2 + 1}{\gamma_P \left(\frac{A_{3.4}}{A_{3.2}}\right)_{CJ} + 1} \right] \quad (53)$$

$$T_{a3.4} = T_{3.2} \left( \frac{C_{P,R}}{C_{P,P}} \right) \left( \frac{1 + \frac{\gamma_R - 1}{2} M_{det}^2 + q}{\frac{\gamma_P + 1}{2}} \right) \quad (54)$$

The static temperature and static pressure are used to calculate the entropy change to station 3.4 based on Eq. 55.

$$\Delta S_{a3.4} = [C_{P,P} \ln(T_{a3.4}) - C_{P,R} \ln(T_{3.2})] - \left[ R_P \ln\left(\frac{P_{a3.4}}{P_0}\right) - R_R \ln\left(\frac{P_{3.2}}{P_0}\right) \right] \quad (55)$$

Kaemming changes the frame of reference from the laboratory frame-of-reference to the detonation wave frame-of-reference using the velocity triangles in Fig. 5 [4]. In the detonation wave frame-of-reference, the ZND detonation model is valid [4; 5; 11]. The velocity of the flow coming into the detonation wave in the detonation frame-of-reference is calculated as a vector sum of the axial velocity and detonation wave velocity, as seen in Eq. 56.

$$V_{3w} = \sqrt{V_{3.2y}^2 + V_{det}^2} \quad (56)$$

Kaemming assumes the circumferential Mach number after the detonation in the detonation wave frame-of-reference  $M_{3.4x,w}$  is one [4]. The circumferential velocity in the detonation wave frame-of-reference is calculated using Eq. 57

$$V_{3.4x,w} = M_{3.4x,w} \sqrt{\gamma_P g_c R_P T_{3.4}} \quad (57)$$

Kaemming converts the static pressure and static temperature calculated in Eq. 53 and Eq. 54

to stagnation in the detonation wave frame-of-reference (which is equivalent to accelerating the flow to the detonation velocity in the laboratory frame-of-reference) to calculate the total temperature in the laboratory frame-of-reference using Eq. 58 [4; 11]. The total temperature calculated in Eq. 58 was compared to the total temperature calculated in Eq. 50 to ensure agreement [4]. The total temperature is used to calculate the total pressure using isentropic relations, as seen in Eq. 59 [21].

$$T_{t,a3.4} = T_{a3.4} + \frac{V_{3.4x,w}^2 - V_{det}^2 + V_{3.2y}^2}{2C_{P,P}} \quad (58)$$

$$P_{t,a3.4} = P_{a3.4} \left( \frac{T_{t,a3.4}}{T_{a3.4}} \right)^{\frac{\gamma_P}{\gamma_P - 1}} \quad (59)$$

The total temperature and total pressure calculated from Eq. 58 and Eq. 59 are used to calculate the total entropy change based on the total properties using Eq. 60.

$$\Delta S_{t,a3.4} = [C_{P,P} \ln(T_{t,a3.4}) - C_{P,R} \ln(T_{3.2})] - \left[ R_P \ln\left(\frac{P_{t,a3.4}}{P_0}\right) - R_R \ln\left(\frac{P_{3.2}}{P_0}\right) \right] \quad (60)$$

The flow traveling along path *a* continues to the exit of the RDE chamber with substation 3.4 properties, as seen in Fig. 7. After exiting the the RDE, the flow is expanded to the throat (station 8), exit (station 9), and ambient using isentropic relations. The circumferential velocity calculated from the empirical model described in Eq. 6 is assumed to remain constant throughout the expansion process because no energy is extracted from the rotating flow [4; 7]. The Mach number at the throat is calculated based on the user-defined axial throat Mach number (assumed to be choked by default from Table 6) and the empirically modeled circumferential velocity, as seen in Eq. 61 [4].

$$M_{a8} = \frac{M_{a8y}}{\left( \sqrt{1 - (\text{Circumferential Velocity Detonated Flow})^2} \right)} \quad (61)$$

The Mach number at the throat is used to calculate the pressure, temperature, and velocity of the flow at the throat using the isentropic relations functions [21]. Kaemming uses the user-defined nozzle stream correction factor ( $C_S$ ) and empirical correction factors from Fig. 10 to calculate the specific thrust using Eq. 62 [3; 4; 14]. The specific thrust is based on the stream thrust function

[22: Eq. 2.92] divided by the mass flow rate equation from Eq. 28. Kaemming uses the mass correction term (Eq. 9) and momentum correction term (Eq. 10) to correct the mass flow rate and specific thrust, respectively [15].

$$\left(\frac{F}{\dot{m}}\right)_{a8} = \frac{C_S \left(\frac{mV}{mV^*}\right) \left(1 + \gamma_P M_{a8y}^2\right) - \frac{P_0}{P_{a8}}}{\left(\frac{m}{m^*}\right) M_{a8y} \left(\frac{\gamma_P g_c}{\sqrt{R_P T_{a8}}}\right)} \quad (62)$$

In rocket engines, the specific impulse is given as the ratio of the thrust to the weight flow of fuel and oxidizer [22]. In air-breathing engines, the specific impulse is given as the ratio of the thrust to the weight flow of the fuel alone [22]. In each case, the specific impulse is based on what the vehicle is required to carry (i.e., both the fuel and oxidizer in the rocket or only fuel in the air-breathing engine). The specific impulse calculated in this thesis is the specific impulse for air-breathing vehicles. The specific impulse for rockets can be found by multiplying the specific thrust by  $\left(\frac{g_c}{g_0}\right)$ . Note that the specific impulse for rockets will have the same magnitude as the specific thrust. The specific impulse for air-breathing engines is calculated using Eq. 63 [3; 4; 14].

$$I_{sp,a8} = \left(\frac{F}{\dot{m}}\right)_{a8} \left(\frac{1 + FAR_{det}}{FAR_{det}}\right) \left(\frac{g_c}{g_0}\right) \quad (63)$$

The flow at the throat is expanded to the exit (station 9). The axial Mach number at the exit  $M_{a9y}$  is calculated using the function `expansion_mode`. The total temperature between stations 8 and 9 is conserved [7; 22], so it is used to calculate a parameter analogous to the circumferential Mach number, as seen in Eq. 64.

$$\left(\frac{V}{a_t}\right)^2 = \frac{V_{a9x}^2}{\gamma_P g_c R_p T_{t,a3.4}} \quad (64)$$

The station 9 Mach number is calculated using Eq. 65, which corrects for the total temperature used in Eq. 64.

$$M_{a9} = \sqrt{\frac{M_{a9y}^2 + \left(\frac{V}{a_t}\right)^2}{1 - \left(\frac{\gamma_P - 1}{2}\right) \left(\frac{V}{a_t}\right)^2}} \quad (65)$$

The exit Mach number  $M_{a9}$  and isentropic relations functions are used to calculate the temperature,

pressure, and speed of sound at station 9 [4; 21]. The station 9 velocity is calculated as the product of the station 9 Mach number and speed of sound. The axial velocity component of the exit flow is calculated using Eq. 66 [4].

$$V_{a9y} = \sqrt{V_{a9}^2 - V_{a9x}^2} \quad (66)$$

The specific thrust and specific impulse are calculated using Eq. 67 and Eq. 68 [3; 4; 14].

$$\left(\frac{F}{\dot{m}}\right)_{a9} = \frac{C_S \left(\frac{mV}{mV^*}\right) \left(1 + \gamma_P M_{a9y}^2\right) - \frac{P_0}{P_{a9}}}{\left(\frac{m}{m^*}\right) M_{a9y} \left(\frac{\gamma_P g_c}{\sqrt{R_P T_{a9}}}\right)} \quad (67)$$

$$I_{sp,a9} = \left(\frac{F}{\dot{m}}\right)_{a9} \left(\frac{1 + FAR_{det}}{FAR_{det}}\right) \left(\frac{g_c}{g_0}\right) \quad (68)$$

To expand the flow to the ambient conditions, the Mach number  $M_{a,amb}$  is calculated using the pressure ratio  $\frac{P_{t,a3.4}}{P_0}$  and the function `M_PtqP`. The Mach number is used to calculate the temperature, area ratio, speed of sound, and velocity using isentropic relations functions [4; 21]. The constant circumferential velocity is again used to remove the circumferential component from the total velocity similar to Eq. 66, resulting in the axial velocity component  $V_{ay,amb}$ . The ideal specific thrust is calculated using Eq. 69 [4; 22]. The associated specific impulse is calculated using Eq. 70.

$$\left(\frac{F}{\dot{m}}\right)_{a,amb} = \frac{V_{ay,amb}}{g_c} \quad (69)$$

$$I_{sp,amb} = \left(\frac{F}{\dot{m}}\right)_{a,amb} \left(\frac{1 + FAR_{det}}{FAR_{det}}\right) \left(\frac{g_c}{g_0}\right) \quad (70)$$

### Path *b*: Detonation and Shock.

In Fig. 7, the flow traveling along path *b* passes through the same detonation between substation 3.2 to *b*3.4 as the flow traveling along path *a* from substation 3.2 to *a*3.4. Therefore, the properties at substation *b*3.4 equal those at substation *a*3.4. Unlike the flow traveling along path *a*, the flow traveling along path *b* passes through an oblique shock between substation *b*3.4 and substation *b*3.6.

Kaemming calculates the Mach number entering the detonation wave in the detonation wave

frame-of-reference using Eq. 71 [4].

$$M_{det,w} = \frac{V_{det}}{\sqrt{\gamma_P g_c R_P T_{3.4}}} \quad (71)$$

The normal component of  $M_{det,w}$  is calculated using the user-defined angle of the shock relative to the flow  $\theta_{shock}$  from Table 6. The shock angle is used to determine the normal component of the Mach number. The normal component of the Mach number is used with the normal shock functions to find the temperature and pressure at station  $b3.6$  [21]. The greater the shock angle, the greater the normal component of the Mach number, and the greater the change in temperature and pressure across the oblique shock [21]. The entropy rise across the shock is calculated using Eq. 72 [4]. The entropy rise across the shock calculated in Eq. 72 is added to the entropy rise across the detonation calculated in Eq. 55 to find the total entropy rise along path  $b$  [4].

$$\Delta S_{b3.6} = C_{P,P} \ln \left( \frac{T_{b3.6}}{T_{b3.4}} \right) - R_P \ln \left( \frac{P_{b3.6}}{P_{b3.4}} \right) \quad (72)$$

The flow traveling along path  $b$  continues to the exit of the RDE chamber with substation  $b3.6$  properties, as seen in Fig. 7. After exiting the the RDE, the flow is expanded to the throat (station 8), exit (station 9), and ambient using isentropic relations (see expansion of path  $a$  flow for process) [4].

### Path c: Deflagration.

Kaemming assumes the ratio of specific heats and gas constant are linear functions of the fuel-to-air ratio [4]. If the detonation fuel-to-air ratio is greater than the deflagration fuel-to-air ratio, the ratio of specific heats and gas constant at station  $c3.4$  are calculated using Eq. 73 and Eq. 74, respectively [4]. If the deflagration fuel-to-air ratio is greater than the detonation fuel-to-air ratio, the ratio of specific heats and gas constant at station  $c3.4$  are calculated using Eq. 75 and Eq. 76, respectively [4].

$$\gamma_{c3.4} = \gamma_{air} + (\gamma_P - \gamma_{air}) \left( \frac{FAR_{defl}}{FAR_{det}} \right) \quad (73)$$

$$R_{c3.4} = R_{air} + (R_P - R_{air}) \left( \frac{FAR_{defl}}{FAR_{det}} \right) \quad (74)$$

$$\gamma_{c3.4} = \gamma_P \quad (75)$$

$$R_{c3.4} = R_P \quad (76)$$

The ratio of specific heats and gas constant are used to calculate molecular weight and specific heat capacity using Eq. 77 and Eq. 78, respectively [4; 21].

$$MW_{c3.4} = \frac{R_U}{R_{c3.4}} \quad (77)$$

$$C_{P,c3.4} = \left( \frac{\gamma_{c3.4}}{\gamma_{c3.4} - 1} \right) R_{c3.4} \quad (78)$$

Kaemming calculates the total temperature at station *c3.4* using Eq. 79, where  $FAR_{min}$  is the the lower of  $FAR_{defl}$  and  $FAR_{det}$  [4].

$$T_{t,c3.4} = \left( \frac{1}{C_{P,c3.4}} \right) \left[ C_{P,R} T_{t3,sum} + \left( \frac{\Delta H}{1 + FAR_{det}} \right) \left( \frac{FAR_{min}}{FAR_{det}} \right) \right] \quad (79)$$

Kaemming assumes the deflagration is a constant pressure process, so the pressure at substation *c3.4* is the same as the pressure at substation 3.2 [4]. The total temperature  $T_{t,c3.4}$  is used with the axial velocity  $V_{3.2y}$  from Eq. 36 to calculate the axial Mach number at station *c3.4* using Eq. 80.

$$M_{c3.4y} = \sqrt{\frac{V_{3.2y}^2}{\gamma_{c3.4} g_c R_{c3.4} T_{tc3.4} - \left( \frac{\gamma_{c3.4}-1}{2} \right) V_{3.2y}^2}} \quad (80)$$

The Mach number is then used to calculate the static temperature using isentropic relations [21]. The entropy rise after deflagration is calculated using Eq. 81 [4].

$$\Delta S_{c3.4} = [C_{P,c3.4} \ln(T_{c3.4}) - C_{P,R} \ln(T_{3.2})] - \left[ R_{c3.4} \ln\left(\frac{P_{c3.4}}{P_0}\right) - R_R \ln\left(\frac{P_{3.2}}{P_0}\right) \right] \quad (81)$$

The flow traveling along path *c* passes through an oblique shock between substations *c3.4* and

*c3.6*, as seen in Fig. 7. Kaemming changes the frame of reference from the laboratory to detonation wave frame-of-reference based on Fig. 5 in order to use normal shock relations [4; 21]. The total velocity of the flow is given by Eq. 56 and the circumferential component is given by  $V_{det}$  from Eq. 52 [4]. The component of the Mach number normal to the oblique shock wave is calculated using Eq. 82 [4].

$$M_{c3.4x} = \frac{V_{c3.4x}}{\sqrt{\gamma_{c3.4} g_c R_{c3.4} T_{c3.4}}} \quad (82)$$

Normal shock relations calculate the static temperature ratio, static pressure ratio, total pressure ratio, and Mach number across the oblique shock to station *c3.6* [21]. The entropy rise to substation *c3.6* is calculated using Eq. 83 [4].

$$\Delta S_{c3.6} = [C_{P,c3.4} \ln(T_{c3.6}) - C_{P,R} \ln(T_{3.2})] - \left[ R_{c3.4} \ln\left(\frac{P_{c3.6}}{P_0}\right) - R_R \ln\left(\frac{P_{3.2}}{P_0}\right) \right] \quad (83)$$

The speed of sound at substation *c3.6* is calculated using Eq. 84.

$$a_{c3.6} = \sqrt{\gamma_{c3.4} g_c R_{c3.4} T_{c3.6}} \quad (84)$$

The circumferential velocity in the detonation wave frame-of-reference  $V_{c3.6x,w}$  is calculated as the product of the Mach number across the oblique shock and  $a_{c3.6}$  from Eq. 84 [4].

The static temperature is converted to stagnation in the detonation wave frame-of-reference to get the total temperature using Eq. 85.

$$T_{t,c3.6} = T_{c3.6} + \frac{V_{c3.6x,w}^2 - V_{det}^2 + V_{3.2y}^2}{2C_{P,c3.4}} \quad (85)$$

The total pressure is calculated using isentropic relations, as seen in Eq. 86 [21].

$$P_{t,c3.6} = P_{c3.6} \left( \frac{T_{t,c3.6}}{T_{c3.6}} \right)^{\frac{\gamma_{c3.4}}{\gamma_{c3.4}-1}} \quad (86)$$

The entropy rise after the shock is calculated using Eq. 87 [4].

$$\Delta S_{t,c3.6} = [C_{P,c3.4} \ln(T_{t,c3.6}) - C_{P,R} \ln(T_{3.2})] - \left[ R_{c3.4} \ln\left(\frac{P_{t,c3.6}}{P_0}\right) - R_R \ln\left(\frac{P_{3.2}}{P_0}\right) \right] \quad (87)$$

### Path *d*: Mixed Flow.

The flow traveling along path *d* is comprised of flow from substations *a3.4*, *b3.6*, and *c3.6*, as seen in Fig. 7. When the three different paths first meet, the parameter  $Z_{defl}$  from Eq. 40 dictates what percentage of the total flow is comprised of flow from path *c*. Kaemming assumes that the remainder of the flow, calculated in Eq. 42, is comprised of equal parts flow *a* and *b* to simplify the analysis [4]. Kaemming uses the empirical models from Fig. 9 to calculate the percentage of the total flow coming from paths *a* and *b* using Eq. 88 and Eq. 89, respectively [4]. The remainder of the flow is comprised of flow from path *d*, as seen in Eq. 90.

$$Z_a = \frac{\dot{m}_a}{\dot{m}_{tot}} = (1 - \text{Detonation Plus Shock Flow Fraction})Z_{det} - 0.5Z_{defl}\text{Relative Mixing} \quad (88)$$

$$Z_b = \frac{\dot{m}_b}{\dot{m}_{tot}} = \text{Detonation Plus Shock Flow Fraction}Z_{det} - 0.5Z_{defl}\text{Relative Mixing} \quad (89)$$

$$Z_d = \frac{\dot{m}_d}{\dot{m}_{tot}} = 1 - Z_a - Z_b \quad (90)$$

Kaemming uses the percentages from Eqs. 88–90 to calculate weighted average values at substation *d3.6* for the ratio of specific heat, specific gas constant, heat capacity, total temperature, and net entropy change using the respective properties from stations *a3.4*, *b3.6*, and *c3.6* [4]. Kaemming uses the weighted entropy change to calculate the total pressure for the flow expanded to station *d3.6* based on Eq. 91 [4].

$$P_{t,d3.6} = P_0 e^{\left\{ \left[ C_{P,d3.6} \ln(T_{t,d3.6}) - C_{P,R} \ln(T_{3.2}) + R_R \ln\left(\frac{P_{3.2}}{P_0}\right) - \Delta S_{d3.6} \right] / R_{d3.6} \right\}} \quad (91)$$

The flow traveling along path *d* continues to the exit of the RDE chamber with substation *d3.6* properties, as seen in Fig. 7. After exiting the RDE, the flow is expanded to the throat (station 8),

exit (station 9), and ambient using isentropic relations (see expansion of path *a* flow for process) [4].

## Exit Flow Model

Kaemming calculates the exit properties for the three exiting paths *a*, *b*, and *d* using weighted averages. The overall fuel-to-air ratio is calculated with percentages from Eq. 40 and Eq. 42 using Eq. 92.

$$FAR_{overall} = Z_{defl}FAR_{defl} + Z_{det}FAR_{det} \quad (92)$$

The specific thrust at the throat  $(\frac{F}{\dot{m}})_{avg,8}$ , the specific thrust at the exit  $(\frac{F}{\dot{m}})_{avg,9}$ , the specific thrust expanded to the ambient  $(\frac{F}{\dot{m}})_{avg,amb}$ , static pressure at the throat  $P_{8,avg}$ , static temperature at the throat  $T_{8,avg}$ , and the total temperature  $T_{t4,avg}$  are calculated using weighted averages with the percentages from Eqs. 88–90. The specific impulse is calculated at the throat, exit, and ambient based on Eq. 93 with *i* replaced with 8, 9, and ambient, respectively [3; 14].

$$I_{sp,avg,i} = \left(\frac{F}{\dot{m}}\right)_{avg,i} \left(\frac{1 + FAR_{overall}}{FAR_{overall}}\right) \left(\frac{g_c}{g_0}\right) \quad (93)$$

The equivalent exhaust velocity is calculated using Eq. 94 [3; 14; 22].

$$V_e = \left(\frac{F}{\dot{m}}\right)_{avg,amb} g_c \quad (94)$$

The equivalent exhaust Mach number based on the velocity from Eq. 94 is calculated using Eq. 95 [4].

$$M_e = \frac{V_e}{\sqrt{\gamma_P g_0 R_P T_{t4,avg} - \left(\frac{F}{\dot{m}}\right)_{avg,amb}^2 \frac{\gamma_P - 1}{2}}} \quad (95)$$

The total exit pressure is calculated using isentropic relations with the equivalent exhaust Mach number from Eq. 95 [4].

## Mass Flow.

All of the flow path calculations are based on percentage of total flow. The throat area is based the the cross-sectional area from Eq. 14, the user-defined ratio of  $\frac{A_8}{A_3}$  from Table 6, and flow coefficient for combustion chamber exit  $C_{W8}$  from Table 6 [4]. The exit mass flow (“w4” in Fig. 11) is calculated using the throat area in the function `find_flow` and correcting the result with the mass correction factor from Eq. 9. The difference between the injection (“w3”) and exit mass (“w4”) flow rate is updated and the iteration cycle varies the pre-detonation pressure  $P_{3.2}$  to equate the two mass flow calculations [4].

## Summary

The NPSS RDE model is composed of four elements: an air source, a fuel source, the RDE, and the exhaust. The flow in the RDE element itself is divided into four paths: detonation, detonation and shock, deflagration, and mixed. The pre-detonation pressure  $P_{3.2}$  is iterated until the entrance and exit model mass flow calculations converge to a consistent solution.

## IV. Analysis and Results

The NPSS model is verified by comparison to the Kaemming model [4] and published CFD results [3; 14]. The default values from Table 6 are the baseline case. The baseline case is the same as the CFD simulations [3; 14], enabling a direct comparison between the models. In all of the following cases, the default values from Table 6 are used for all parameters except for the parameter being varied.

The specific impulses in all of the following cases is calculated for air-breathing engines using the weight of the fuel alone. The specific impulse for rocket engines will have the same magnitude as the specific thrust, but with units of seconds. The use of both specific impulse calculations allows the RDE to be compared to both air-breathing engines and rocket engines.

### Comparison to Kaemming Model

The average specific impulse expanded to the ambient from Eq. 93 is used as the metric of comparison because small changes are amplified due to the  $\frac{1+FAR_{overall}}{FAR_{overall}}$  term ( $\frac{1+FAR_{overall}}{FAR_{overall}} \approx 35$  in the default case). Since both the Kaemming and NPSS models were developed similarly, the results were expected to be the same. The only differences would arise from any inherent numerical precision differences between Microsoft Excel and NPSS.

Figures 12–15 illustrate four parametric variations to demonstrate agreement between the two models. Figures 12 and 13 vary the geometry of the RDE via the height and the mean throughflow diameter, respectively. Figures 14 and 15 vary the thermodynamic inputs of the RDE via the entrance pressure ( $P_{t3}$ ) of the air and fuel and the entrance temperature ( $T_{t3}$ ) of the air and fuel, respectively. In the analysis, the entrance pressure and temperature for the air and fuel are both assumed to be equal (i.e.,  $P_{t3,air} = P_{t3,fuel}$  and  $T_{t3,air} = T_{t3,fuel}$ ) to simplify the analysis. As expected, the results of the Kaemming model matched the results of the NPSS model.

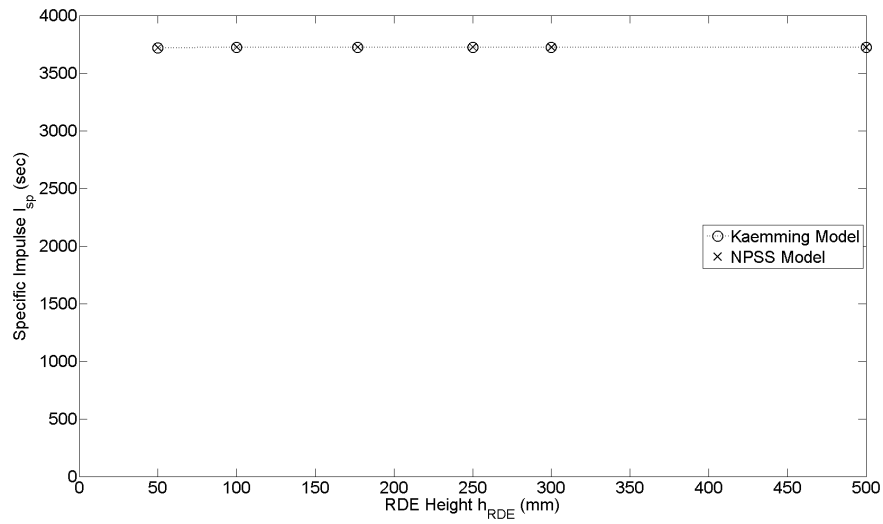


**Figure 12.** Parametric variation of RDE height and specific impulse ( $D_m = 140$  mm,  $P_{t3} = 58.784$  psia, and  $T_{t3} = 540$  R)

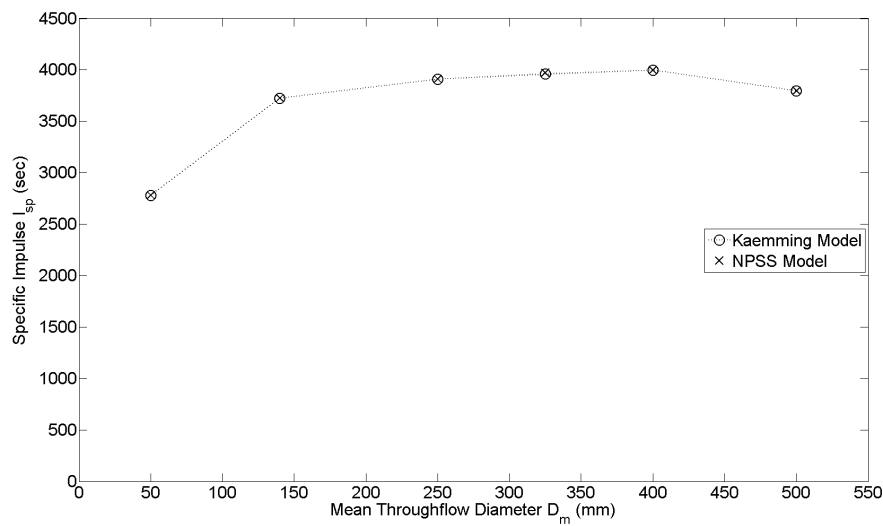


**Figure 13.** Parametric variation of mean throughflow diameter and specific impulse ( $h_{RDE} = 237$  mm,  $P_{t3} = 58.784$  psia, and  $T_{t3} = 540$  R)

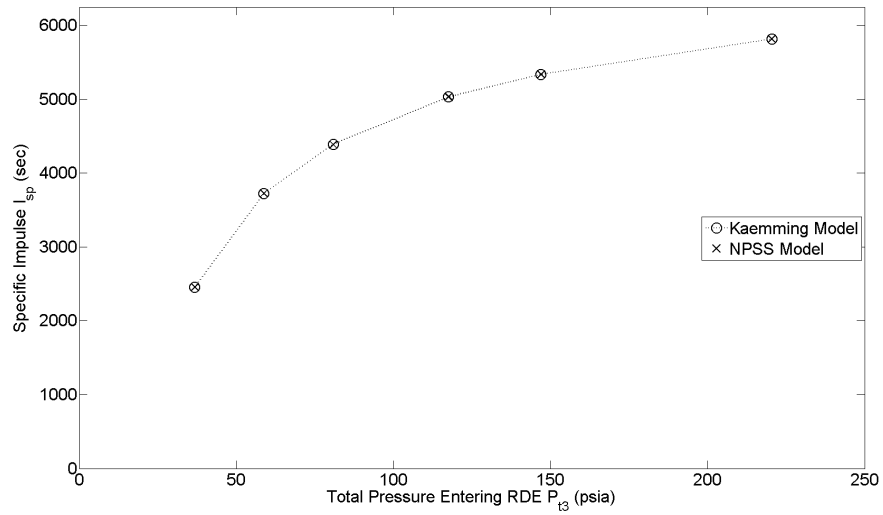


**Figure 14.** Parametric variation of entrance pressure and specific impulse ( $h_{RDE} = 237 \text{ mm}$ ,  $D_m = 140 \text{ mm}$ , and  $T_{t3} = 540 \text{ R}$ )

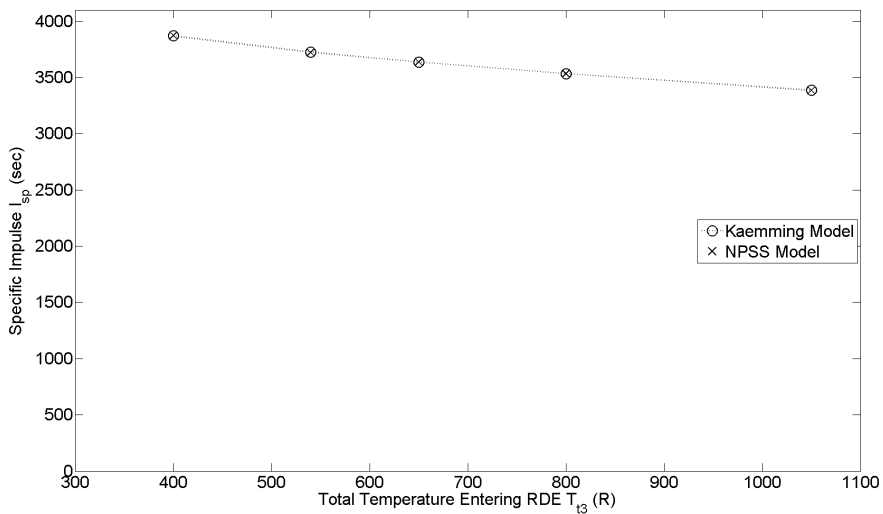


**Figure 15.** Parametric variation of entrance temperature and specific impulse ( $h_{RDE} = 237 \text{ mm}$ ,  $D_m = 140 \text{ mm}$ , and  $P_{t3} = 58.784 \text{ psia}$ )

## Comparison to CFD Simulations

The NPSS model was compared to published CFD results [3; 14]. The parametric variation of RDE height from Fig. 12 is compared to CFD results [14: Fig. 10] in Fig. 16.

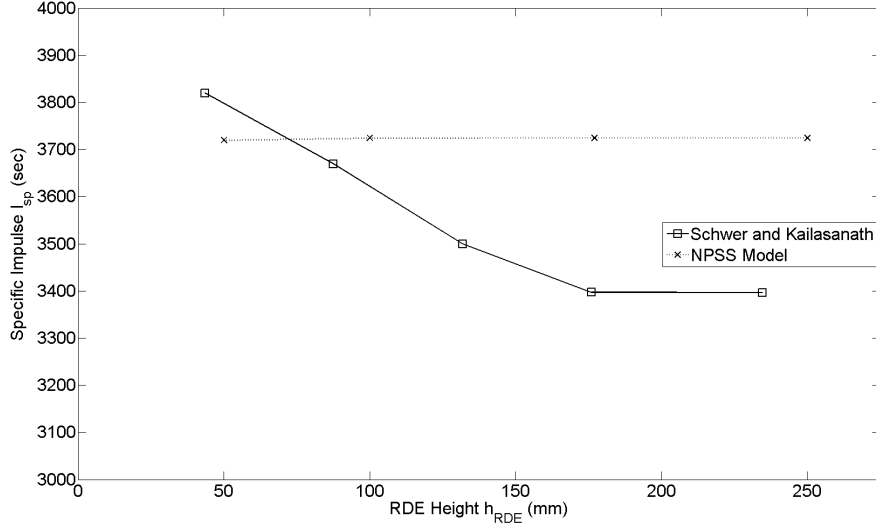


**Figure 16. Comparison of the RDE height variation from NPSS model to published results ( $D_m = 140$  mm,  $P_{t3} = 58.784$  psia, and  $T_{t3} = 540$  R)**

The specific impulse calculated from the NPSS model is seemingly invariant with RDE height, while the CFD simulation shows an inverse relationship between specific impulse and RDE height. Kaemming suggests higher order interactions (e.g., non-linearity of the empirical models from Fig. 9, calorically imperfect gas effects, diffusion) take place in the CFD simulations which lower the specific impulse [4]. Nonetheless, the greatest deviation between the NPSS model and the CFD simulation is 330 sec, which represents a 9.7% difference. While the NPSS model does not follow the CFD exactly, it provides a sufficient approximation.

The parametric variation of the mean throughflow diameter from Fig. 13 uses an entrance pressure of 58.784 psia, as seen in Table 6. However, CFD simulation results for the mean throughflow diameter use an entrance pressure of 147 psia [14]. The NPSS parametric variation of the mean throughflow diameter in Fig. 17 also uses an entrance pressure of 147 psia and is compared to CFD results [14: Fig. 8].

The specific impulses calculated from the variation of mean diameter in the NPSS model agree

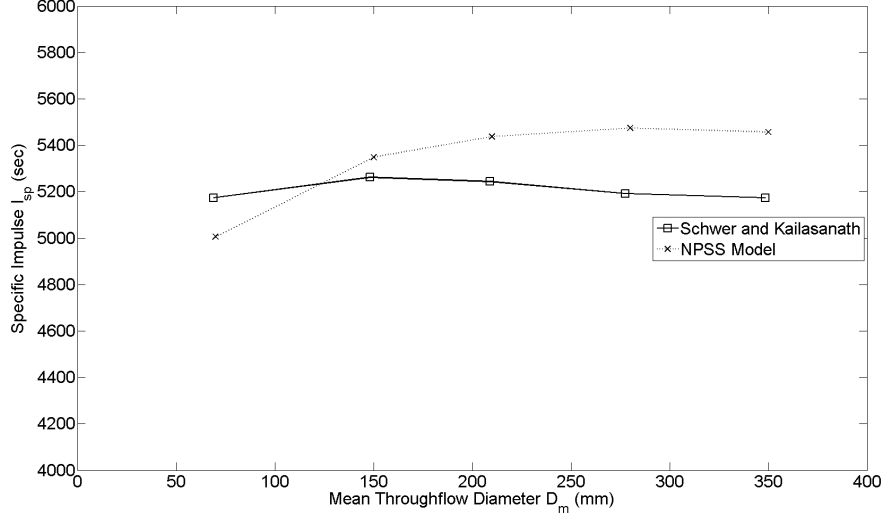


**Figure 17.** Comparison of the RDE mean throughflow diameter variation from NPSS model to published results ( $h_{RDE} = 237$  mm,  $P_{t3} = 147$  psia, and  $T_{t3} = 540$  R)

fairly well with the CFD simulations. The greatest difference of 280 sec represents a 5.5% difference.

The ratio of the entrance pressure to the ambient pressure ( $P_{t3}/P_0$ ) is used to compare the results from the NPSS model to CFD simulation [3; Table 2] in Fig. 18. In both the NPSS model and CFD simulations, the ambient pressure is  $P_0 = 14.7$  psia [3; 4]. Besides the lowest pressure

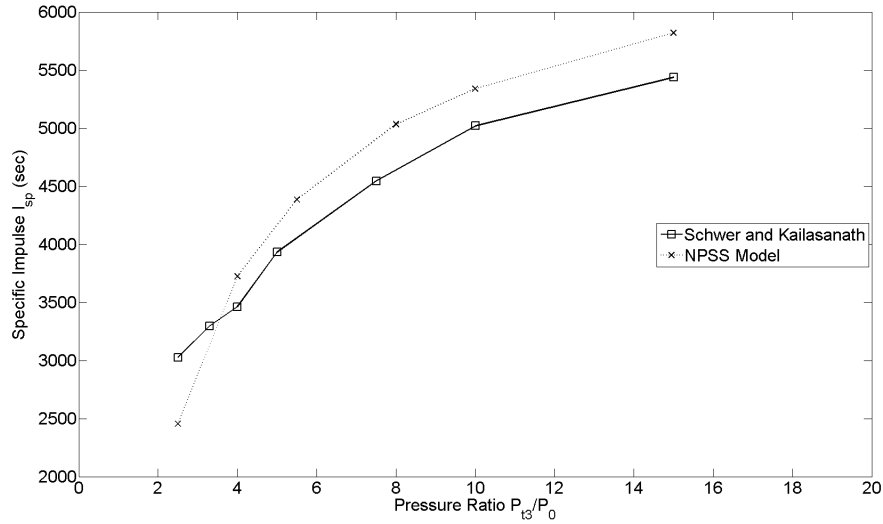


**Figure 18.** Comparison of  $P_{t3}/P_0$  from NPSS model to published results ( $h_{RDE} = 237$  mm,  $D_m = 140$  mm,  $P_0 = 14.7$  psia, and  $T_{t3} = 540$  R)

ratio of  $P_{t3}/P_0 = 2.5$ , the NPSS model consistently calculates a higher specific impulse than the

CFD simulation. However, the greatest difference of 380 sec represents a 7.0% difference, which represents a fair approximation.

The NPSS model does not provide the complex flowfield visualizations and distribution profiles for properties of interest like the CFD simulations seen in Fig. 2 and Fig. 3. However, the NPSS model executes significantly faster (less than 5 sec) and requires fewer computational resources than the CFD simulations while providing a sufficient approximation.

## Model Application

The NPSS model was found to agree with the Kaemming model [4] and published CFD simulation results [3; 14]. The NPSS model is then used to illustrate why an iterative method was required to determine  $P_{3,2}$  as well as the effects of the shock angle  $\theta_{shock}$ . Finally, the NPSS model is used to further analyze the RDE in a rocket configuration.

As previously mentioned, the pre-combustion pressure  $P_{3,2}$  is iterated in the RDE model. A parametric variation of the entrance total pressure and entrance total temperature with the pre-combustion pressure is illustrated in Fig. 19.

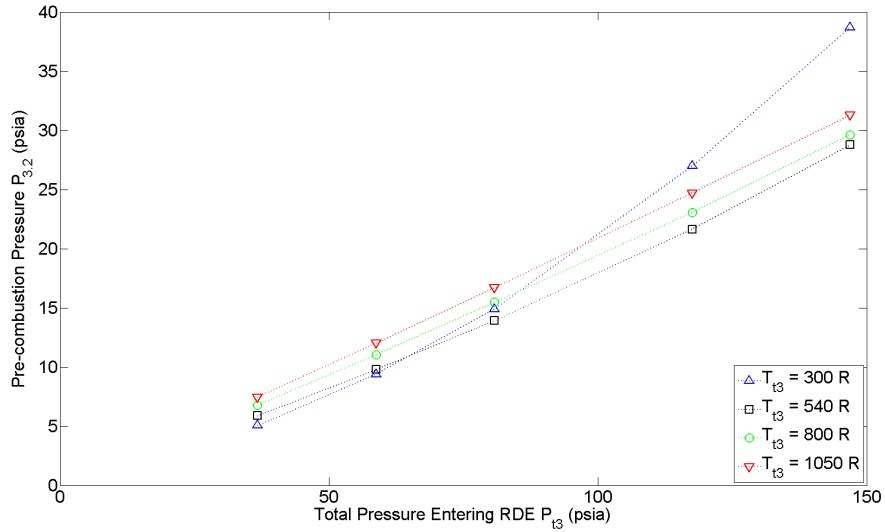


**Figure 19. Parametric variation of entrance total pressure and entrance total temperature with the pre-combustion pressure ( $h_{RDE} = 237\text{ mm}$  and  $D_m = 140\text{ mm}$ )**

As seen in Fig. 19, the relationship between the entrance total pressure, entrance total

temperature, and pre-combustion pressure is complex. At a total entrance temperature of 300 R, the relationship between the entrance total pressure and pre-combustion pressure is non-linear, while at a total entrance temperature of 1050 R, the relationship is approximately linear. Due to the complex relationship between the three parameters, an empirical model has not yet been developed and the iterative process is required.

Kaemming uses a shock angle of  $\theta_{shock} = 60^\circ$  as the angle of the shock relative to the flow [4], as described in Table 6. A parametric analysis of the shock angle with the total pressure and total temperature exiting the RDE is illustrated in Fig. 20. A parametric analysis of the shock angle with the specific thrust and specific impulse is illustrated in Fig. 21.

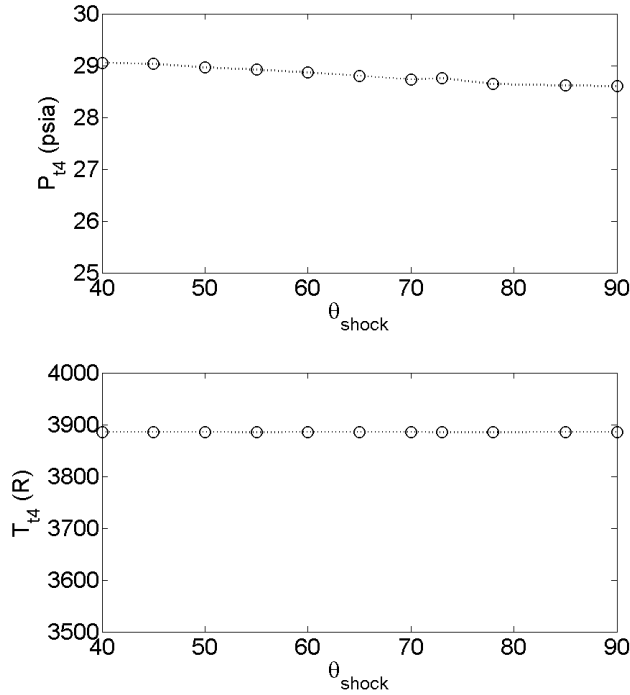


**Figure 20. Parametric analysis of shock angle with the exit total pressure and total temperature ( $h_{RDE} = 237$  mm,  $D_m = 140$  mm,  $P_{t3} = 58.784$  psia, and  $T_{t3} = 540$  R)**

As seen in Fig. 20, the shock angle  $\theta_{shock}$  does not significantly affect the total pressure and total temperature exiting the RDE. The total pressure changes less than 1.5% and the total temperature changes less than 0.003% across a wide range of shock angles. As seen in Fig. 21, the shock angle  $\theta_{shock}$  does not significantly affect the specific thrust or specific impulse. The specific thrust changes less than 1% and the specific impulse changes less than 1.5% across a wide range of shock angles.

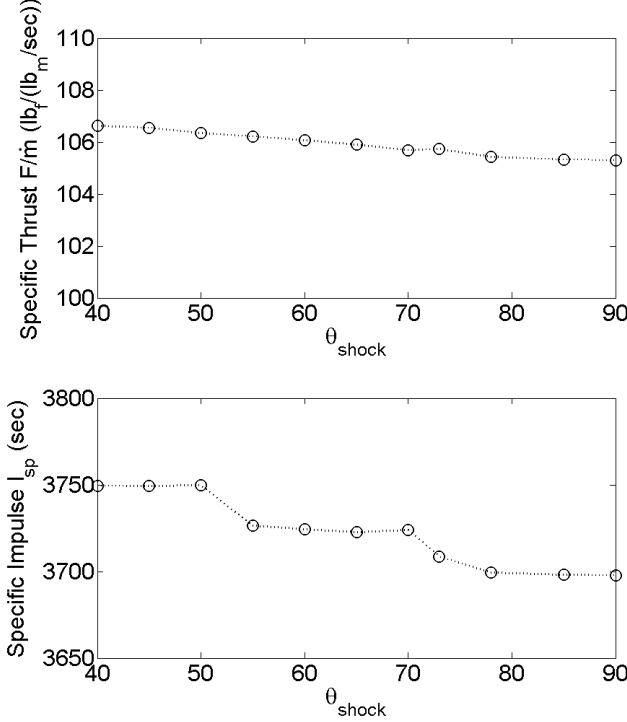


**Figure 21. Parametric analysis of shock angle with the specific thrust and specific impulse ( $h_{RDE} = 237 \text{ mm}$ ,  $D_m = 140 \text{ mm}$ ,  $P_{t3} = 58.784 \text{ psia}$ , and  $T_{t3} = 540 \text{ R}$ )**

Therefore, if there is a deviation from from the assumed  $60^\circ$ , the effect is negligible.

The effect of RDE geometry (specifically, the RDE height and mean throughflow diameter) on the specific thrust and specific impulse is illustrated in Fig. 22 and Fig. 23, respectively.

As with the parametric analysis of the RDE height in Fig. 12, the specific thrust in Fig. 22 and the specific impulse in Fig. 23 reach plateaus. Additional RDE height will not provide any more specific thrust or specific impulse, so for weight savings, only the shortest required RDE should be used in a rocket. In the plateaus, the RDE has extracted as much energy from the fuel as possible, so additional time in the combustion chamber will not yield additional energy extraction. As the mean throughflow diameter increases, a greater RDE height is required to reach the plateau. As the mean throughflow diameter increases, the mass flow passing through the RDE also increases. The greater mass flow requires additional time in the combustion chamber for the RDE to extract maximum energy. Additionally, as the mean throughflow diameter increases, the plateau values increase. It follows that as the mass flow increases, the total amount of energy extracted increases.

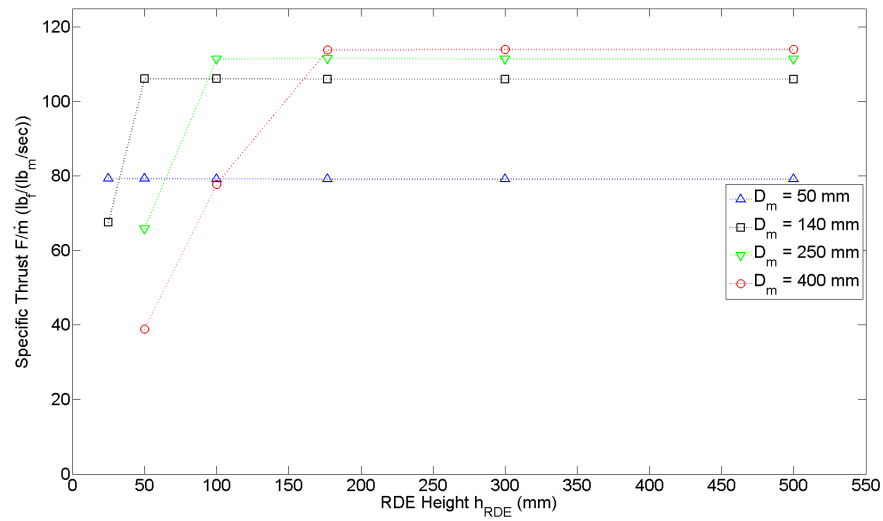


**Figure 22. Parametric analysis of RDE height and mean throughflow diameter on specific thrust ( $P_{t3} = 58.784 \text{ psia}$ , and  $T_{t3} = 540 \text{ R}$ )**

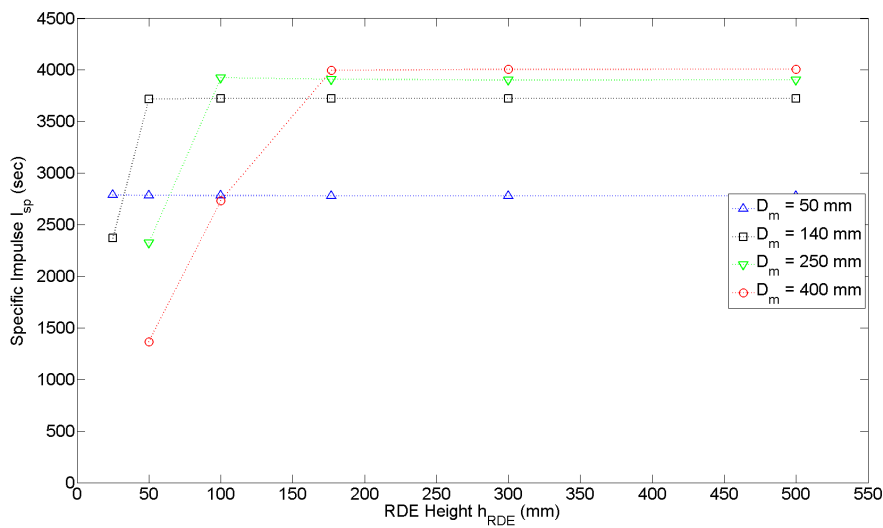


**Figure 23. Parametric analysis of RDE height and mean throughflow diameter on specific impulse ( $P_{t3} = 58.784 \text{ psia}$ , and  $T_{t3} = 540 \text{ R}$ )**

Figure 24 illustrates the relationship between mean throughflow diameter, RDE height, and mass flow rate. As seen in Fig. 24, the mass flow rate is invariant with the RDE height and has

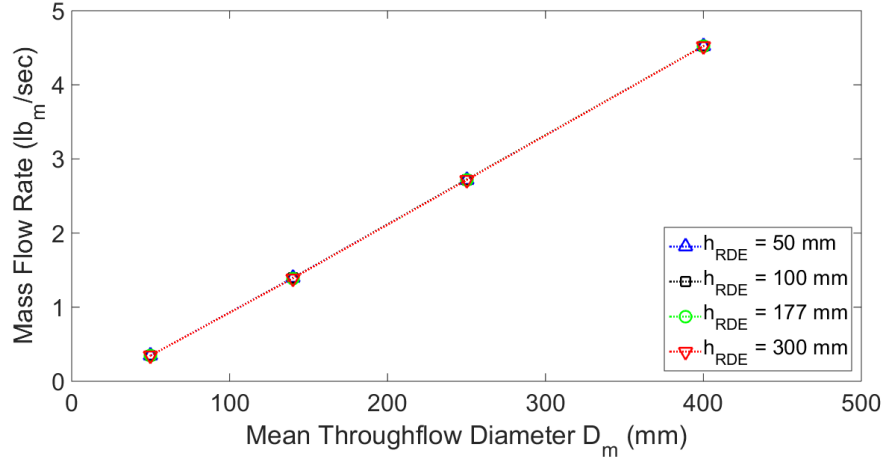


**Figure 24.** Parametric analysis of RDE height and mean throughflow diameter on mass flow rate ( $P_{t3} = 58.784 \text{ psia}$ , and  $T_{t3} = 540 \text{ R}$ )

a linear relationship with the mean throughflow diameter. The linear relationship between mean throughflow diameter and mass flow rate provides a simple scaling model that can be used to determine the desired size of an RDE.

Figure 25 illustrates the relationship between mean throughflow diameter, RDE height, and thrust. After a certain height, the specific thrust in Fig. 22 and the thrust in Fig. 25 both reach

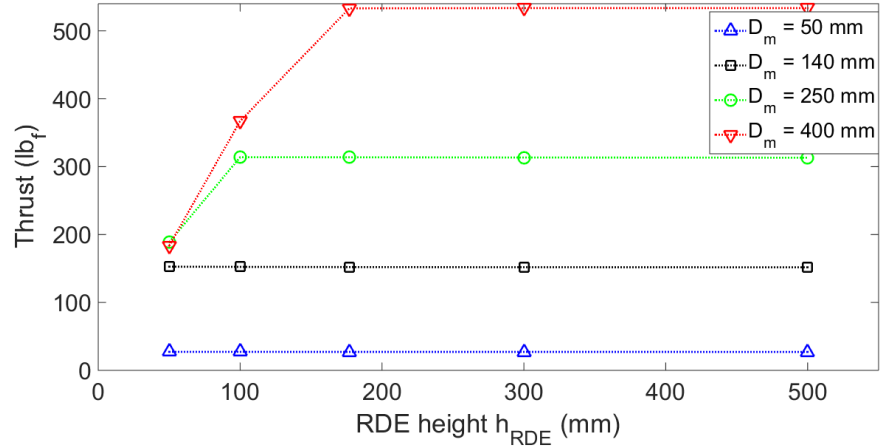


**Figure 25.** Parametric analysis of RDE height and mean throughflow diameter on thrust ( $P_{t3} = 58.784 \text{ psia}$ , and  $T_{t3} = 540 \text{ R}$ )

plateaus. In designing an RDE, only the minimum required RDE height (i.e., the height where the

specific thrust and thrust reach plateaus) should be used; there are no additional gains from a taller RDE. In Fig. 22, increasing the mean throughflow diameter results in decreasing gains in specific thrust. In Fig. 25, however, increasing the mean throughflow diameter results in increasing gains in the thrust. Based on Figs. 22–25, the mean throughflow diameter is the key sizing parameter.

The combined effect of total entrance temperature and total entrance pressure on the specific thrust and specific impulse is illustrated in Fig. 26 and Fig. 27, respectively.

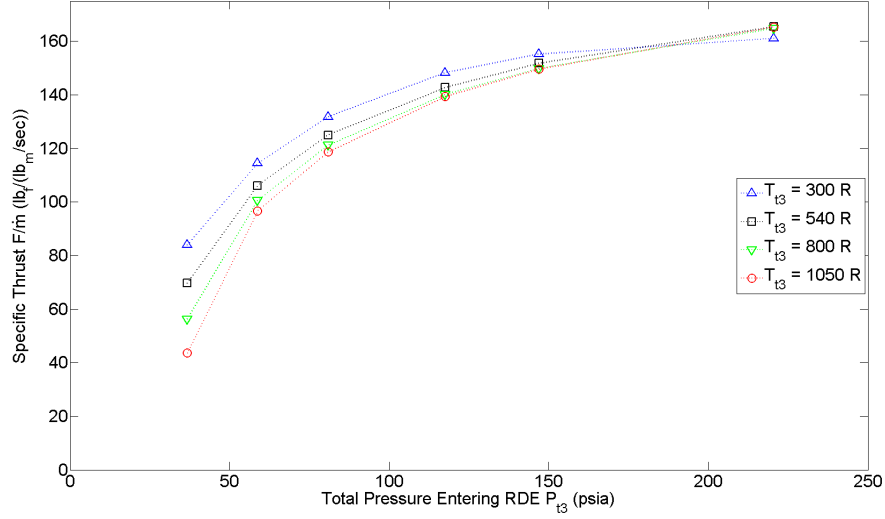


**Figure 26. Parametric analysis of total entrance temperature and total pressure on specific thrust ( $h_{RDE} = 237\text{ mm}$  and  $D_m = 140\text{ mm}$ )**

At the lower entrance pressures, the total entrance temperature has a significant effect on the specific thrust and specific impulse. As the entrance total pressure increases, the total entrance temperature has less of an effect. Increasing the total entrance temperature decreases the specific thrust and specific impulse for the different total entrance pressures. The specific thrust and specific impulse are increasing at a decreasing rate and appear to be trending towards plateaus at  $150 \frac{\text{lb}_f}{\text{lb}_m/\text{s}}$  and  $5500 \text{ sec}$ , respectively.

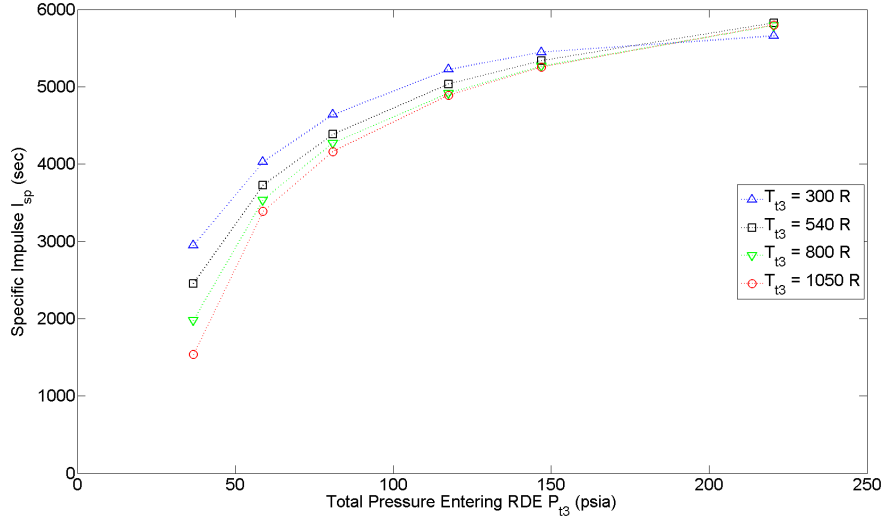


**Figure 27. Parametric analysis of total entrance temperature and total pressure on specific impulse ( $h_{RDE} = 237 \text{ mm}$  and  $D_m = 140 \text{ mm}$ )**

The combined effect total entrance temperature and total entrance pressure on the mass flow is illustrated in Fig. 28. The mass flow rate from Fig. 28 is used with the specific thrust from Fig. 26

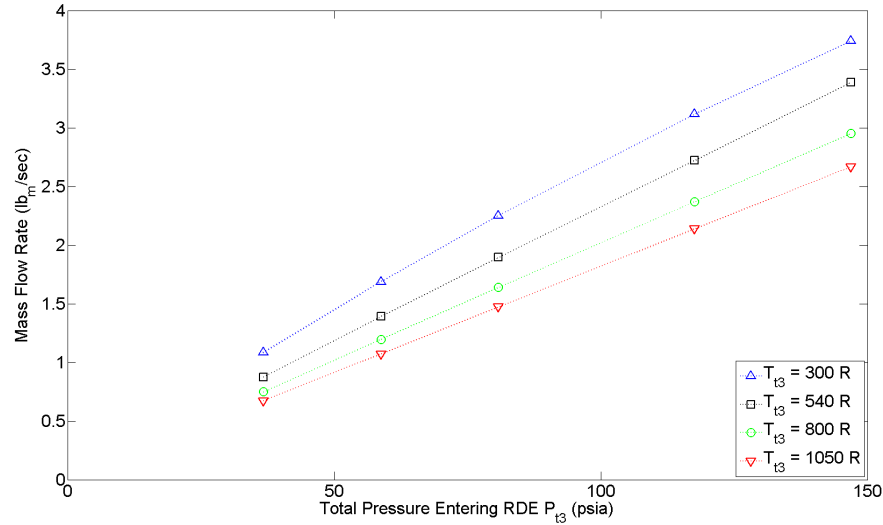


**Figure 28. Parametric analysis of total entrance temperature and total pressure on mass flow rate ( $h_{RDE} = 237 \text{ mm}$  and  $D_m = 140 \text{ mm}$ )**

to calculate the total thrust, as seen in Fig. 29.

Both the mass flow rate in Fig. 28 and thrust in Fig. 29 increase linearly with the total entrance pressure. The entrance total temperature affects the slope of each line, and at a higher total entrance

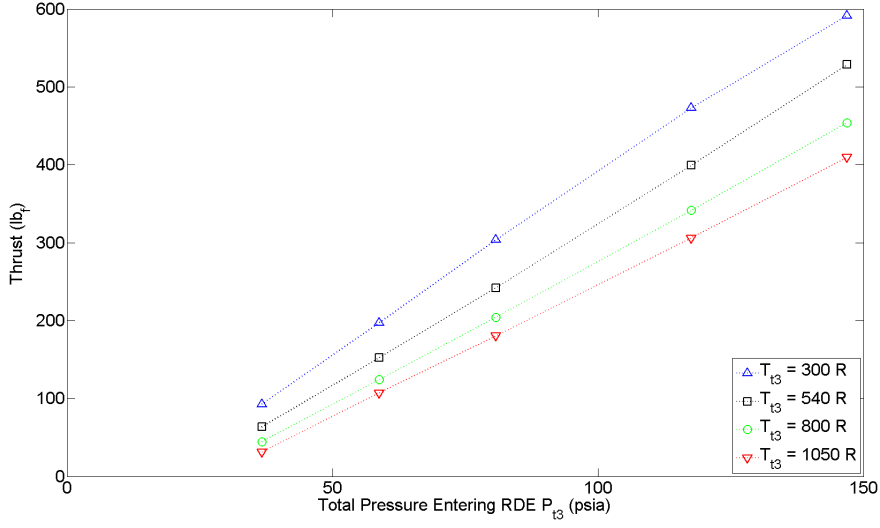


**Figure 29.** Parametric analysis of total entrance temperature and total pressure on thrust ( $h_{RDE} = 237\text{ mm}$  and  $D_m = 140\text{ mm}$ )

pressure, the total entrance temperature has a greater impact. Even if the specific thrust plateaus as in Fig. 26, the increasing mass flow rate will increase the net thrust.

Material properties often limit the temperature exiting the combustor in traditional engines [7]. Therefore, the temperature exiting the RDE  $T_{t4}$  is a parameter of concern. The effect of total entrance temperature  $T_{t3}$  and total entrance pressure  $P_{t3}$  on total exit temperature  $T_{t4}$  is illustrated in Fig. 30.

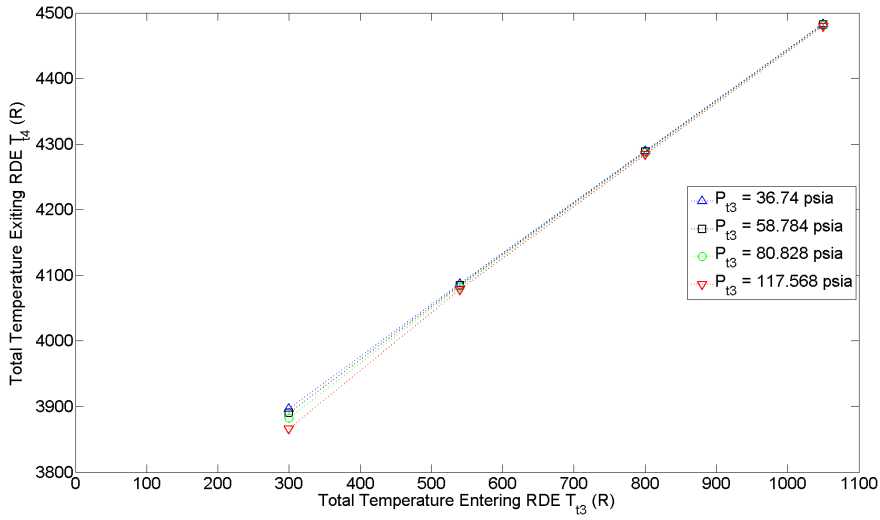


**Figure 30.** Parametric analysis of total entrance temperature and total pressure on total exit temperature ( $h_{RDE} = 237\text{ mm}$  and  $D_m = 140\text{ mm}$ )

The total entrance pressure has a negligible effect on the total exit temperature. There is a linear relationship between the total entrance temperature and total exit temperature. Temperatures of 3000  $R$  to 4700  $R$  exist in real rocket engines [22], though material developments may lead to higher allowable temperatures. The total exit temperatures in Fig. 30 fall within the range of existing rocket exhaust temperatures; however, cooling will still be a concern.

The RDE is a pressure-gaining combustor, which is why the RDE is able to achieve the higher efficiency of the Atkinson cycle [3; 11; 13; 14]. The pressure ratio across the RDE is given in Eq. 96.

$$\pi_b = \frac{P_{t8}}{P_{t,3.2}} \quad (96)$$

The parametric variation of  $\pi_b$  with total entrance pressure and total entrance temperature is illustrated in Fig. 31. The value of  $\pi_b = 1$  is shown to illustrate that all pressure ratios are greater than one.

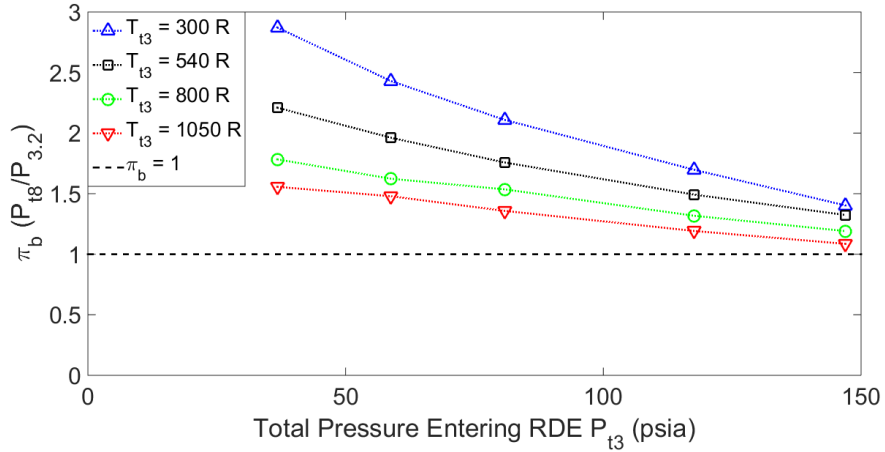


**Figure 31. Parametric variation of  $\pi_b$  with total entrance pressure and total entrance temperature ( $h_{RDE} = 237$  mm and  $D_m = 140$  mm)**

As seen in Fig. 31, the RDE produces a pressure rise across the entire range of pressures and temperatures implemented. The pressure rise agrees with CFD simulations [11; 14]. Therefore, the RDE does, in fact, follow the Atkinson cycle and will be able to realize the higher thermal efficiency [3; 11; 13; 14].

The pressure profile from Fig. 8 results in a pressure loss across the plenum from station 3 to

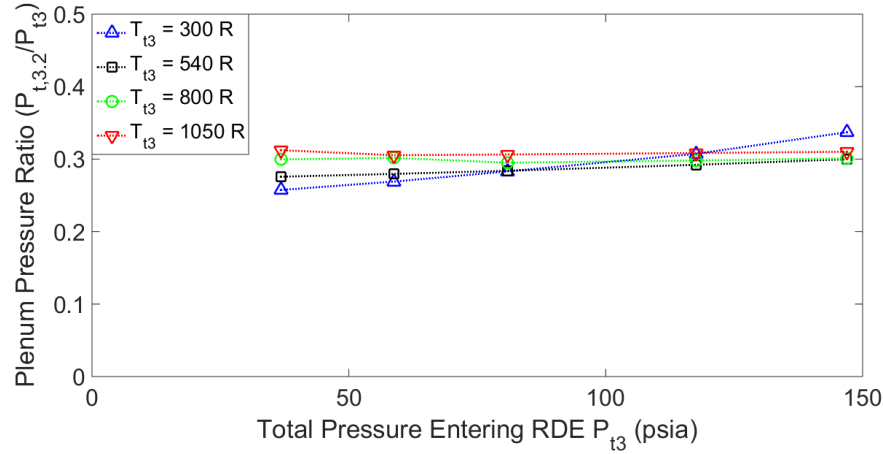


**Figure 32. Parametric variation of plenum pressure loss with total entrance pressure and total entrance temperature ( $h_{RDE} = 237 \text{ mm}$  and  $D_m = 140 \text{ mm}$ )**

substation 3.2. The parametric variation of the plenum pressure loss with total entrance pressure and total entrance temperature is illustrated in Fig. 32.

As seen in Fig. 32, the pressure loss is significant; the total pressure that enters the RDE combustion chamber (substation 3.2) is only 25% to 35% of the total pressure entering the RDE (station 3). Some of the pressure loss can be attributed to feedback from the injectors [17]. Detailed analysis of the pressure loss across the plenum requires further investigation and is outside the scope of this thesis.

### Investigative Questions Answered

The highest specific thrust calculated is just over  $150 \frac{lb_f}{lb_m/sec}$  and the highest specific impulse is approximately  $5,500 \text{ sec}$ , as seen in Fig. 26 and Fig. 27, respectively. Again, the specific impulse is force per weight flow of fuel alone. The specific impulse based on total air and fuel weight flow, for comparison to other rocket propulsion methods, is  $150 \text{ sec}$ .

The specific impulse for a traditional turbojet using hydrogen fuel can range from  $4,500 \text{ sec}$  to  $7,000 \text{ sec}$  [23]. The calculated RDE specific impulse for air-breathing engines of  $5,500 \text{ sec}$  falls within the range of turbojet engines. A typical rocket engine using liquid hydrogen fuel has a specific impulse of  $410 \text{ sec}$  [22: Table 1.6]. The calculated RDE specific impulse for rocket engines

of 150 sec falls below that of existing rocket engines. The nozzle and exhaust were assumed to be ideal, as were the internal flows between the air and fuel sources into the RDE. The RDE requires further investigation in order to improve the performance of the RDE. In a real RDE, the specific impulse will be lower due to losses, but the results are still very promising and merit continued development of the RDE in a rocket configuration.

## Summary

The NPSS model was verified by comparison to the Kaemming model [4] and published CFD results [3; 14]. The NPSS model matched the Kaemming model. The NPSS model matched CFD simulations closely with a maximum difference of 10%. The calculated specific impulses of the RDE peaked at 5,500 sec when based on the weight flow of fuel alone and 150 sec when based on the weight flow of fuel and air. The promising results merit continued development of the RDE model and development of a real RDE in a rocket configuration for comparison.

## V. Conclusions and Recommendations

Detonation-based combustion follows an Atkinson cycle and has a higher inherent thermodynamic efficiency than deflagration-based combustion following a Brayton cycle [8]. The parametric variations in this thesis calculated that the RDE had an air-breathing engine specific impulse that fell in the range of traditional turbojets using hydrogen fuel and a rocket engine specific impulse that fell below hydrogen-oxygen rockets. Nonetheless, the advantages of the RDE are numerous. For one, a higher specific impulse would require a lower mass flow to produce the same amount of thrust [22], and lower mass flow translates to a lower total required fuel load.

### Recommendations for Future Research

There are two main categories for recommendations: model development and model application. Model development describes improvements that can be made to the NPSS model. Model application describes possible uses for the NPSS model.

#### Model Development.

While the simplified NPSS model agrees with the CFD simulations, it has not been compared to experimental results. The empirical models are based exclusively on results from higher-order CFD simulations [3; 14]. Additionally, the exit flow boundary conditions in the CFD simulations are still a matter of debate [3; 4; 14]. The empirical models, and thus the entire RDE model, would be further improved if experimental results were incorporated into their development. Including experimental results would also validate the code.

The NPSS model is programmed using iterative loops. The mass flows for air and fuel are calculated in those iterative loops, as are the fuel-to-air ratios for the deflagrated and detonated flows. Additionally, the inlet flow conditions (e.g., pressure, temperature) are coded into RDE element. The NPSS environment allows for all those parameters to be defined outside the RDE element in the air and fuel inlet elements. Also, NPSS contains solvers to facilitate the iteration

loops. However, the current code does not incorporate these capabilities. Future improvements to the code should incorporate the NPSS capabilities to simplify the code and speed up calculations.

Finally, the RDE model assumes the flow is calorically perfect and has constant chemical composition [4]. In traditional deflagration combustion cycle analysis, equilibrium chemistry is often assumed for a more accurate calculation [4; 18]. Equilibrium chemistry should be an incorporated capability of the RDE model.

## Model Application.

The rocket configuration outlined in this thesis is a starting point for the implementation of the RDE. Further analysis should be accomplished on the different configuration options. Several configurations utilizing a generic combustor have been developed [16]. The RDE model can be used in conjunction with a compressor to increase the pressure going into the RDE. Another option is to couple the RDE with a traditional rocket engine so the RDE can be used in parallel with the traditional combustor to create additional thrust. Alternatively, it can be used in an afterburner-like capacity to further increase thrust.

A final potential use for the RDE is in a traditional turbojet engine. It can be used to replace the burner and compressor in the engine, or just the burner itself. Alternatively, it could be used as a secondary combustor, either in parallel with a traditional combustor in an afterburner-like capacity.

The NPSS RDE element allows the various configurations to be readily modeled. The analysis could be used to find optimal design and operating conditions for the RDE. Additionally, the analyses would provide a more direct comparison between traditional engines and those modified with an RDE.

## Summary

The RDE provides promising results that merit further development. The implemented empirical models and gas dynamic properties can be improved with experimental results to provide more

accurate results. The internal structure of the RDE code can be improved and simplified by using some of the built-in NPSS features. The NPSS RDE element allows the various configurations to be readily modeled to find optimal design and operating conditions for their various uses.

## Appendix A. Summary of Implemented Functions

Several functions are implemented for repeated calculations. Functions are coded in the same manner to subroutines. The key difference is that functions return values and subroutines do not; in the RDE element, all functions are of type `real`, while all subroutines are of type `void`. The functions were used to perform common thermodynamic calculations.

### Isentropic Relations

The functions `PtqP` and `TtqT` solved for the isentropic total/static pressure and temperature ratios, respectively. The isentropic total/static pressure was calculated based on Eq. A.1 [21: Eq. (44)].

$$\frac{P_t}{P} = \left( 1 + \left( \frac{\gamma - 1}{2} \right) M^2 \right)^{\frac{\gamma}{\gamma-1}} \quad (\text{A.1})$$

The isentropic total/static temperature was calculated based on Eq. A.2 [21: Eq. (43)].

$$\frac{T_t}{T} = 1 + \left( \frac{\gamma - 1}{2} \right) M^2 \quad (\text{A.2})$$

The functions `M_PtqP` and `M_TtqT` solved for the Mach number based on the isentropic total/static pressure and temperature ratios, respectively, based on Eqs. A.3 and A.4, respectively.

$$M = \sqrt{\left( \frac{2}{\gamma - 1} \right) \left[ \left( \frac{P_t}{P} \right)^{\frac{\gamma-1}{\gamma}} - 1 \right]} \quad (\text{A.3})$$

$$M = \sqrt{\left( \frac{2}{\gamma - 1} \right) \left( \frac{T_t}{T} - 1 \right)} \quad (\text{A.4})$$

The function `AqAstar` solved for the isentropic area ratio for chocked flow in a nozzle, based on Eq. A.5 [21: Eq. (80)].

$$\frac{A}{A^*} = \left( \frac{1}{M} \right) \left\{ \left[ \frac{2}{\gamma - 1} \right] \left( 1 + \left( \frac{\gamma - 1}{2} \right) M^2 \right) \right\}^{\frac{\gamma+1}{2(\gamma-1)}} \quad (\text{A.5})$$

The functions `Msub_A` and `Msup_A` utilize the function `AqAstar` to iteratively calculate the Mach number based on the isentropic area ratio and produce the subsonic and supersonic solution, respectively.

## Normal Shock Relations

The functions `P2qP1ns`, `Pt2qPt1ns`, `T2qT1ns`, and `M2ns` calculated flow properties across a normal shock. The static pressure ratio across a normal shock was calculated by the function `P2qP1ns` using Eq. A.6 [21: Eq. (93)].

$$\frac{P_2}{P_1} = \frac{2\gamma M^2 - (\gamma - 1)}{\gamma + 1} \quad (\text{A.6})$$

The total pressure ratio across a normal shock was calculated by the function `Pt2qPt1ns` using Eq. A.7 [21: Eq. (99)].

$$\frac{P_{t2}}{P_{t1}} = \left[ \frac{(\gamma + 1)M^2}{(\gamma - 1)M^2 + 2} \right]^{\frac{\gamma}{\gamma-1}} \left[ \frac{\gamma + 1}{2\gamma M^2 - (\gamma - 1)} \right]^{\frac{1}{\gamma-1}} \quad (\text{A.7})$$

The static temperature ratio across a normal shock was calculated by the function `T2qT1ns` using Eq. A.8 [21: Eq. (95)].

$$\frac{T_2}{T_1} = \frac{[2\gamma M^2 - (\gamma - 1)][(\gamma - 1)M^2 + 2]}{(\gamma + 1)^2 M^2} \quad (\text{A.8})$$

The Mach number across a normal shock was calculated by the function `M2ns` using Eq. A.9 [21: Eq. (96)].

$$M_2 = \sqrt{\frac{(\gamma - 1)M_1^2 + 2}{2\gamma M_1^2 - (\gamma - 1)}} \quad (\text{A.9})$$

## Mass Flow

The function `find_flow` iterates total mass flow to match a desired total area for three separate flows. The function uses the desired flow area and three arrays containing the density, velocity, and flow percentages of each of the three streams. The area contribution each of the flows made was

calculated using Eq. A.10.

$$A_i = \frac{\dot{m}_{tot}(\% \text{ flow})_i}{\rho_i V_i} \quad (\text{A.10})$$

The total mass flow was iterated until the desired total area  $A_{tot}$  was attained by Eq. A.11.

$$A_{tot} = A_1 + A_2 + A_3 \quad (\text{A.11})$$

## Nozzle Expansion

The function `expansion_mode` finds the exit Mach number for a flow expanding from the throat to exit (station 8 to station 9) by first calculating the isentropic area ratio  $\frac{A_8}{A^*}$ , and then  $\frac{A_9}{A^*}$  using Eq. A.12.

$$\frac{A_9}{A^*} = \left( \frac{A_9}{A_8} \right) \left( \frac{A_8}{A^*} \right) \quad (\text{A.12})$$

The subsonic Mach number at station 9 was calculated using `Msub_A`. The subsonic Mach number was used to calculate  $P_9$  using Eq. A.13.

$$P_9 = P_8 \left( \frac{\frac{P_{t8}}{P_8}}{\frac{P_{t9}}{P_9}} \right) \quad (\text{A.13})$$

The calculated pressure  $P_9$  was compared to the ambient pressure: if it was less than or equal to the ambient pressure  $P_0$ , the expansion was subsonic.

If the calculated pressure  $P_9$  was greater than the ambient pressure  $P_0$ , the expansion was supersonic. The supersonic Mach number at station 9 was calculated using `Msup_A`, and the pressure at station 9 was calculated using Eq. A.13. The normal shock wave was accounted for by multiplying the calculated pressure by the appropriate factor for a normal shock using the function `P2qP1ns`. If the calculated pressure  $P_9$  after the normal shock was still greater than the ambient pressure  $P_0$ , the nozzle was fully supersonic.

If the calculated pressure  $P_9$  after the normal shock was less than the ambient pressure  $P_0$ , the nozzle was overexpanded and there was a shock in the nozzle. The equation used to find the exit Mach number was derived from the continuity equation (*i.e.*,  $\dot{m}_8 = \dot{m}_9$ ), based on Eq. A.14

[7: Eq. (1.4)].

$$\dot{m} = P A M \sqrt{\frac{\gamma g_0}{R T_t} \left[ 1 + \left( \frac{\gamma - 1}{2} \right) M^2 \right]} \quad (\text{A.14})$$

Assuming the ratio of specific heats and the gas constant remain constant during the expansion, the full continuity equation becomes Eq. A.15.

$$P_8 A_8 M_8 \sqrt{\frac{\gamma g_0}{R T_{t8}} \left[ 1 + \left( \frac{\gamma - 1}{2} \right) M_8^2 \right]} = P_9 A_9 M_9 \sqrt{\frac{\gamma g_0}{R T_{t9}} \left[ 1 + \left( \frac{\gamma - 1}{2} \right) M_9^2 \right]} \quad (\text{A.15})$$

The pressure at the exit was equal to the ambient pressure ( $P_9 = P_0$ ). Assuming choked flow at the nozzle ( $M_8 = 1$ ) and adiabatic expansion ( $T_{t8} = T_{t9}$ ), the equation reduces to Eq. A.16.

$$P_8 A_8 \sqrt{\left( \frac{\gamma + 1}{2} \right)} = P_0 A_9 M_9 \sqrt{\left[ 1 + \left( \frac{\gamma - 1}{2} \right) M_9^2 \right]} \quad (\text{A.16})$$

Squaring both sides and rearranging leads to Eq. A.17, which was used to iteratively solve for  $M_9$ .

$$M_9^2 \left[ \left( \frac{\gamma - 1}{2} \right) M_9^2 + 1 \right] = \left[ \left( \frac{P_8}{P_0} \right) \left( \frac{A_8}{A_9} \right) \right]^2 \left( \frac{\gamma + 1}{2} \right) \quad (\text{A.17})$$

## Chapman-Jouguet with Area Relief

The function `CJ_mach_area` found the Chapman-Jouguet Mach number for a flow with two different values of  $\gamma$  and a changing area. A steady, one-dimensional detonation propagates at a sonic velocity at the Chapman-Jouguet state [19]. In the rotating detonation engine, however, there is lateral relief after the detonation which provides another source of energy relief [4]. The lateral relief mode was modeled by an increase in area after the detonation, which produced the slower detonation and decreased pressure rise provided by the lateral relief [4].

The mass, momentum, and energy conservation equations were implemented with a change in area and gas properties from state 1 to 2. The equations of conservation of mass, momentum, and

energy became Eqs. A.18, A.19, and A.20, respectively [4].

$$P_1 A_1 M_1 \sqrt{\frac{\gamma_1 g_0}{R_1 T_1}} = P_2 A_2 M_2 \sqrt{\frac{\gamma_2 g_0}{R_2 T_2}} \quad (\text{A.18})$$

$$P_1 A_1 (1 + \gamma_1 M_1^2) = P_2 A_2 \left( \frac{A_1}{A_2} + \gamma_2 M_2^2 \right) \quad (\text{A.19})$$

$$C_{P1} T_1 \left[ 1 + \left( \frac{\gamma_1 - 1}{2} \right) M_1^2 + q \right] = C_{P2} T_2 \left[ 1 + \left( \frac{\gamma_2 - 1}{2} \right) M_2^2 \right] \quad (\text{A.20})$$

In the CFD simulations, the heat of combustion is corrected to stoichiometric heat addition per total reactant flow. The traditional heat of combustion  $\Delta H$  of the fuel is related to the heat of combustion referenced to fuel flow  $\Delta H_v$  and stoichiometric heat of combustion  $\Delta H_{stoich}$  in Eq. A.21 [4; 15; 18].

$$m_{fuel} \Delta H_v = (m_{air} + m_{fuel}) \Delta H = (m_{air} + m_{fuel}) \left( \frac{\Delta H_{stoich}}{m_{f,stoich}} \right) m_f \quad (\text{A.21})$$

Dividing Eq. A.21 by the mass of air results in Eq. A.22.

$$FAR_{det} \Delta H_v = (1 + FAR_{det}) \Delta H = (1 + FAR_{det}) \Delta H_{stoich} \left( \frac{FAR_{det}}{FAR_{stoich}} \right) \quad (\text{A.22})$$

Kaemming defines the non-dimensional heat addition term  $q$  in Eq. A.20 as Eq. A.23 using the same values for  $C_{P,1}$  and  $T_1$  as in Eq. A.20 [4; 15].

$$q = \frac{FAR_{det} \Delta H_v}{C_{P,1} T_1} \quad (\text{A.23})$$

Using the definitions from Eq. A.22, Eq. A.23 can be rewritten using known properties, as seen in Eq. A.24.

$$q = \frac{\Delta H (1 + FAR_{det})}{C_{P,1} T_1} \quad (\text{A.24})$$

The Mach number at station 2 was fixed to one because the detonation moves sonically [4; 18;

19]. Rearranging Eq. A.20 to solve for the temperature ratio leads to Eq. A.25

$$\frac{T_2}{T_1} = \left( \frac{C_{P1}}{C_{P2}} \right) \left[ \frac{1 + \left( \frac{\gamma_1 - 1}{2} \right) M_1^2 + q}{\frac{\gamma_2 + 1}{2}} \right] \quad (\text{A.25})$$

Dividing Eq. A.18 by Eq. A.19 results in Eq. A.26.

$$\left( \frac{1 + \gamma_1 M_1^2}{M_1} \right) \sqrt{\left( \frac{R_2}{R_1} \right) \left( \frac{\gamma_1}{\gamma_2} \right)} = \left( \frac{A_1}{A_2} + \gamma_2 \right) \sqrt{\frac{T_2}{T_1}} \quad (\text{A.26})$$

Substituting Eq. A.25 into Eq. A.26 and using the relation  $\frac{C_P}{R} = \frac{\gamma}{\gamma - 1}$  [21: Eq. (16)] results in Eq. A.27 [4].

$$\frac{1 + \gamma_1 M_1^2}{M_1} = \left( \frac{A_1}{A_2} + \gamma_2 \right) \left( \frac{\gamma_1}{\gamma_2} \right) \sqrt{\left( \frac{\gamma_2 - 1}{\gamma_1 - 1} \right) \left[ \frac{1 + \left( \frac{\gamma_1 - 1}{2} \right) M_1^2 + q}{\frac{\gamma_2 + 1}{2}} \right]} \quad (\text{A.27})$$

The function `CJ_mach_area` iterates  $M_1$  to satisfy the Eq. A.27.

## Interpolation

NPSS allows for lookup and interpolation in tables, but does not allow for arrays to be converted into tables. The function `OneDNtrp` was used to interpolate within an array. The function went through each cell of the independent array to determine which two cells the desired value was between. Then, it interpolated for the desired value in the corresponding dependent array. The function also allowed for extrapolation; however, since all of the implementations of the function were for a bounded range for a ratio between zero and one, no extrapolation was utilized.

## References

1. Daniel Paxson. RDE Thermodynamic Cycle Model Status. Private communication, November 2013.
2. Craig A Nordeen, Douglas Schwer, Fredrick Schauer, John Hoke, Baki Cetegen, and Thomas Barber. Thermodynamic Modeling of a Rotating Detonation Engine. In *49th AIAA Aerospace Sciences Meeting, Orlando, FL*, Orlando, FL, January 2011. American Institute of Aeronautics and Astronautics.
3. Douglas A Schwer and Kailas Kailasanath. Numerical Investigation of Rotating Detonation Engines. *AIAA Paper 2010-6880*, 2010.
4. Tom Kaemming. A User's Guide to a Rotating Detonation Engine Thermodynamic Cycle Performance Code. Version Q. Draft. Also refers to associated Microsoft Excel code., 2014.
5. Craig A Nordeen, Douglas Schwer, Fredrick Schauer, John Hoke, B Cetegen, and T Barber. Divergence and Mixing in a Rotating Detonation Engine. In *51st AIAA Aerospace Sciences Meeting*, Grapevine, TX, January 2013. American Institute of Aeronautics and Astronautics.
6. Z. Spakovszky. Thermodynamics and Propulsion. Online, 2007. Available at <http://web.mit.edu/16.unified/www/SPRING/propulsion/notes/node27.html>.
7. Jack Mattingly. *Aircraft Engine Design*. American Institute of Aeronautics and Astronautics, Reston, VA, 2002. ISBN 9781563475382.
8. Daniel E Paxson. *A Simplified Model for Detonation Based Pressure-Gain Combustors*. National Aeronautics and Space Administration, Glenn Research Center, 2010.
9. BV Voitsekhovskii. Maintained Detonations. *Soviet Physics Doklady*, 4, 1960.
10. Frank K Lu and Eric M Braun. Rotating Detonation Wave Propulsion: Experimental Challenges, Modeling, and Engine Concepts. *Journal of Propulsion and Power*, 30(5):1125–1142, 2014.
11. Craig A Nordeen. *Thermodynamics of a Rotating Detonation Engine*. PhD thesis, University of Connecticut, 2013.
12. K Kailasanath. The Rotating-Detonation-Wave Engine Concept: A Brief Status Report. In *49th AIAA Aerospace Sci. Meeting*, Orlando, FL, January 2011. American Institute of Aeronautics and Astronautics.
13. Craig A Nordeen, Douglas Schwer, Fredrick Schauer, John Hoke, Baki Cetegen, and Thomas Barber. Energy Transfer in a Rotating Detonation Engine. In *47th AIAA Joint Propulsion Conference*, San Diego, CA, August 2011. American Institute of Aeronautics and Astronautics.
14. Douglas A Schwer and Kailas Kailasanath. Numerical Study of the Effects of Engine Size on Rotating Detonation Engines. In *49th AIAA Aerospace Sciences Meeting*, Orlando, FL, January 2011. American Institute of Aeronautics and Astronautics.

15. Tom Kaemming. RE: Cold Flow. Private communication, January 2015.
16. Thomas A Kaemming, Gary L Lidstone, and Brad C Sammann. Proposed Nomenclature Guide for Pulse Detonation Engines. In *38th AIAA/ASME/SAE/ASEE Joint Propulsion Conference and Exhibit*, Indianapolis, IN, July 2002. American Institute of Aeronautics and Astronautics.
17. Douglas A Schwer and Kailas Kailasanath. Feedback into Mixture Plenums in Rotating Detonation Engines. In *50th AIAA Aerospace Sciences Meeting including the New Horizons Forum and Aerospace Exposition*, Nashville, TN, January 2012. American Institute of Aeronautics and Astronautics.
18. Stephen Turns. *An Introduction to Combustion: Concepts and Applications*. McGraw-Hill, New York, 3 edition, 2012. ISBN 9780073380193.
19. Paul W Cooper. *Explosives Engineering*. Wiley-VCH, New York, 1996.
20. Jozef Jarosinski. *Combustion Phenomena Selected Mechanisms of Flame Formation, Propagation, and Extinction*. CRC Press, Boca Raton, 2009. ISBN 9780849384097.
21. Ames Research Staff. Equations, Tables, and Charts for Compressible Flow. Technical Report 1135, National Advisory Committee for Aeronautics, 1953.
22. Jack Mattingly. *Elements of Propulsion: Gas Turbines and Rockets*. American Institute of Aeronautics and Astronautics, Reston, VA, 2006. ISBN 9781563477799.
23. The University of Texas at Arlington Aerodynamic Research Center. Pulsed Detonation Engines. Online, 2014. Available at <http://arc.uta.edu/research/pde.htm>.

## **Vita**

First Lieutenant Nihar N. Shah graduated in 2011 from Rensselaer Polytechnic Institute in Troy, NY with a Bachelor of Science degree in aeronautical and mechanical engineering. He was commissioned as a second lieutenant in the United States Air Force at Detachment 550 AFROTC at Rensselaer Polytechnic Institute. His first assignment was to the Air Force Test and Evaluation Center Detachment 5 at Edwards AFB as an operational test engineer focusing on communication system upgrades on bomber aircraft. In August of 2013, Lieutenant Shah entered the Air Force Institute of Technology in pursuit of a Master of Science degree in aeronautical engineering. Upon graduation, he will be assigned to the National Air and Space Intelligence Center.

# REPORT DOCUMENTATION PAGE

*Form Approved  
OMB No. 0704-0188*

The public reporting burden for this collection of information is estimated to average 1 hour per response, including the time for reviewing instructions, searching existing data sources, gathering and maintaining the data needed, and completing and reviewing the collection of information. Send comments regarding this burden estimate or any other aspect of this collection of information, including suggestions for reducing this burden to Department of Defense, Washington Headquarters Services, Directorate for Information Operations and Reports (0704-0188), 1215 Jefferson Davis Highway, Suite 1204, Arlington, VA 22202-4302. Respondents should be aware that notwithstanding any other provision of law, no person shall be subject to any penalty for failing to comply with a collection of information if it does not display a currently valid OMB control number. PLEASE DO NOT RETURN YOUR FORM TO THE ABOVE ADDRESS.

<b>1. REPORT DATE (DD-MM-YYYY)</b> 26-03-2015	<b>2. REPORT TYPE</b> Master's Thesis	<b>3. DATES COVERED (From — To)</b> Sept 2013 — Mar 2015		
<b>4. TITLE AND SUBTITLE</b>  Computer Modeling of a Rotating Detonation Engine in a Rocket Configuration		<b>5a. CONTRACT NUMBER</b>  <b>5b. GRANT NUMBER</b>  <b>5c. PROGRAM ELEMENT NUMBER</b>		
<b>6. AUTHOR(S)</b>  Shah, Nihar		<b>5d. PROJECT NUMBER</b>  <b>5e. TASK NUMBER</b>  <b>5f. WORK UNIT NUMBER</b>		
<b>7. PERFORMING ORGANIZATION NAME(S) AND ADDRESS(ES)</b>  Air Force Institute of Technology Graduate School of Engineering and Management (AFIT/EN) 2950 Hobson Way WPAFB OH 45433-7765		<b>8. PERFORMING ORGANIZATION REPORT NUMBER</b>  AFIT-ENY-MS-15-M-230		
<b>9. SPONSORING / MONITORING AGENCY NAME(S) AND ADDRESS(ES)</b>  Air Force Research Lab Aerospace Directorate Combustion Branch, Turbine Engine Division 1790 Loop Road North WPAFB OH 45433-7765		<b>10. SPONSOR/MONITOR'S ACRONYM(S)</b>  AFRL/RQTC		
		<b>11. SPONSOR/MONITOR'S REPORT NUMBER(S)</b>		
<b>12. DISTRIBUTION / AVAILABILITY STATEMENT</b>  DISTRIBUTION STATEMENT A: APPROVED FOR PUBLIC RELEASE; DISTRIBUTION UNLIMITED.				
<b>13. SUPPLEMENTARY NOTES</b>  This work is declared a work of the U.S. Government and is not subject to copyright protection in the United States.				
<b>14. ABSTRACT</b>  Detonation-based combustors leverage the higher thermodynamic efficiency of the Atkinson cycle compared to the traditional deflagration-based combustion of the Brayton cycle. The rotating detonation engine (RDE) has one or more shock waves rotating around an annulus. The RDE can theoretically be 20% more thermally efficient than a traditional deflagration-based cycle. A RDE was modeled in Numerical Propulsion System Simulation (NPSS) based on a model developed in Microsoft Excel. The thermodynamic analysis of the RDE in these models is broken into four streams. Empirical models were used to find the percentage of the total flow in each stream. The pre-detonation pressure was iterated until the entrance mass flow calculations matched the exit mass flow calculations. A parametric analysis was used to compare the variation in specific impulse from the NPSS model to the Microsoft Excel model and other published results. The RDE has a peak air-breathing engine specific impulse of approximately 5,500 sec and a peak rocket engine specific impulse of approximately 150 sec.				
<b>15. SUBJECT TERMS</b>  Rotating Detonation Engine, Pressure-Gain Combustor, Atkinson Cycle, Detonation Waves, Combustion, Thermodynamic Cycles, Rocket Engines				
<b>16. SECURITY CLASSIFICATION OF:</b>		<b>17. LIMITATION OF ABSTRACT</b>  U	<b>18. NUMBER OF PAGES</b>  83	<b>19a. NAME OF RESPONSIBLE PERSON</b>  Dr. P. I. King, AFIT/ENY
<b>a. REPORT</b> U	<b>b. ABSTRACT</b> U			<b>c. THIS PAGE</b> U